University of Crete
Department of Physics

Institute of Electronic
Structure and Laser

Electrical impedance spectroscopy of relative humidity sensors based on $NiPS_3$

Natalia Armaou

Master's Thesis

Supervisor: Dr. Deligeorgis George

Abstract

Resistive humidity sensors have been extensively explored, because of their signal stability and low hysteresis, as well as their uses in medicine, environmental monitoring, and wearable electronics. In recent humidity sensors, research has focused on the study and application of two-dimensional materials, as they present unique properties compared to their three-dimensional counterparts, due to their low surface to volume ratio. A new family of two-dimensional materials, transition metal phosphorus trichalcogenides MPX_3, are important candidates for the fabrication of sensors for various applications. In previous work we observed the structural characteristics of the material by changing parameters in the fabrication process, such as the applied power and the duration of the sonication, and also the solvent in use. Here, we explore the deposition of the material and we perform electrical characterization using I-V measurements and Electrical Impedance Spectroscopy (EIS) in a humidity and temperature controlled environment. EIS is widely used to investigate the electrical behavior of the sensor in a range of frequencies, understand the physical mechanisms of detection that are taking place, and fabricate the equivalent circuit for further integrated electrical analysis. Our goal is to connect the electrical performance with the applied parameters of the fabrication process, and as a result we will be able to fabricate novel relative humidity sensors with improved characteristics such as better sensitivity, shorter response and recovery times, and easy repeatability in manufacturing.

Acknowledgments

Firstly, I would like to express my deep appreciation to my scientific supervisor Dr. Deligeorgis George, for the cooperation we had the last three years. Without his patient guidance and support, nothing of these would be possible.

I would like to express my gratitude to Prof. Eleftherios Iliopoulos and Prof. Liverios Lymperakis. I am very lucky to have such supportive and remarkable people as my Master's Thesis Committee.

I am very grateful for being part of the group "Carbon and 2D Electronics", which gave me the opportunity to cooperate with extraordinary people of different disciplines and explore the world of research in Microelectronics. I would like to express special thanks to George Makris for the construction of the relative humidity control set up, which allowed us to characterize our sensors, Dimitris Kosmidis for his valuable assistance and advice in the ESL lab, and of course Alexia Papadopoulou and Sofia Spinthaki for their continuous support and fruitful conversations.

Furthermore, I would like to offer my spacial thanks to my friends Alexandros Spiliotis, Christina Siaitanidou, Nikos Chatzarakis, Nassia Tsiatsiana, Ioannis Balas, Erwin Armiaou, and of course my beloved family for their endless support and encouragement the last two years in my Master's Degree in "Photonics and Nanoelectronics".

Last but not least, I would like to express my gratitude to my uncle Dimitris Katagas for being the reason for me to become a physicist. He will always be my biggest inspiration and I will never forget our endless conversations about the magic of our world.

Table of Contents

1 Introduction

Humidity sensors are necessary in many applications of modern reality. Humidity measurement is used in many fields such as agriculture, medicine, the electrical industry as well as the Internet of Things. In fact the need for protection against environmental conditions has led to the development of various types of humidity sensors using different operating principles, different materials, and structural features.

In recent years, efforts have been made to manufacture sensors with better performance in terms of parameters such as sensitivity, power consumption, and capability for mass production. An important factor for modern technology is the miniaturization of the components in a circuit, as it offers advantages such as low hysteresis, faster response and recovery times, and more efficient spatial integration in a system. For these reasons a large part of modern research has focused on the study of lower – dimensional materials, i.e. two-dimensional (e.g. graphene), one-dimensional (e.g. carbon nanotubes) and zero-dimensional (quantum dots). Specifically in the case of sensors, considering that humidity is detected by the surface of the material, 2D materials have an inherent advantage as they present high surface to volume ratio, and that leads to a sensitive and extremely fast detection.

Electrical impedance spectroscopy (EIS) is a high performance and non-invasive characterization technique. EIS is based on applying a small excitation signal (voltage) and measuring, for a range of frequencies, the amplitude and phase of the current going through the sample, providing a complex impedance spectrum. This technique helps to realize a better characterization of the phenomena taking place, and provides the ability to separate effects having linearly independent dispersions and dominating in different frequency ranges. By performing impedance spectroscopy, it becomes possible to reduce the influence of random deviation, and to benefit from a detailed modeling of the characteristics as the frequency-dependent transfer function of the system is determined. In material science, EIS is sensitive to both surface phenomena and changes of bulk properties including conduction mechanisms, characterize quantitative corrosion processes as well as percolation.[1] [2] It is also extremely useful in characterization of sensors and biosensors because of the dependence of their electrical properties on their interaction with their environment [3] [4] and it has been extensively utilized for battery characterization, as a diagnostic tool and accurate analytical technique for measuring different critical battery parameters. [5] [6]

2 Theory

2.1 Relative humidity Sensors

2.1.1 Relative humidity – Definition

The first humidity sensor made was in 1937 by Francis Dunmore using two wires made of noble metal, which were immersed into a solution of lithium chloride LiCl. Lithium chloride is hygroscopic, and thus has the ability to bind water molecules from the environment, inducing a change of its resistance. More specifically the logarithm of the resistance varied approximately in proportion to the logarithm of the relative humidity.[7] However, due to low sensitivity and long response and recovery times, the need of alternative solutions was raised.[8]

Figure 1: Dunmore Hygrometer Sensor. Reprinted:
https://commons.wikimedia.org/wiki/File:Dunmore_Hygrometer_Sensor_1938.jpg

Humidity is defined as the concentration of water vapor in a quantity of air or some other gas. Different ways of measuring humidity have been developed in order to measure different humidity parameters. The most common are: Relative Humidity (RH), parts per million by volume or by mass, and the dew and frost points. The last two are subcategories of Absolute Humidity.

Absolute Humidity is the ratio of the mass of water vapor per unit volume:

$$AB = \frac{m_w}{V} \quad , \quad [\frac{gr}{m^3}]$$

m_W being the mass of water and V the volume of air. The amount of water vapor the air can hold is a function of temperature and the maximum value is given by the Magnus – Tetens equation:

$$e_s(T) = 6{,}1094 \exp\left(\frac{17{,}625T}{T+243.04}\right)$$

T being the temperature in degrees Celsius and e_s the maximum water vapour pressure in hPa.

Relative Humidity is defined as the ratio of the amount of water vapor pressure the air contains to the amount of maximum water vapor the air can hold under certain temperature and pressure.

$$RH\,\% = \frac{P_V}{P_S} 100$$

P_V the water vapor pressure measured in the air and P_S the water vapor pressure of saturated air.

Dry air has 0% relative humidity, while saturated air has 100%. It is important to note that as the air temperature decreases, the value of relative humidity increases, since the amount of water vapor the air can hold until saturation decreases.

Saturation humidity is defined as the mass of water vapor in saturated air to its volume:

$$SH = \frac{m_{WS}}{V} \quad , \quad \left[\frac{gr}{m^3}\right]$$

Therefore another definition that can be derived for relative humidity is:

$$RH\,\% = \frac{AB}{SH} 100$$

When it comes to Absolute Humidity measurements, the most common parameters measured, as mentioned above, are: the humidity (in parts per million) by volume or by mass, and the dew and frost points. The humidity in parts per million by volume, is the volume of water vapor contained in the air in relation to the volume of dry air, and the mass, respectively, and it is obtained by multiplying the humidity in parts per million by volume, by the ratio of the molecular weight of water to the molecular weight of air (or gas). The dew point is the temperature at which the water vapor contained in the air begins to condense into liquid form. Thus, the dew point corresponds to the relative humidity value of 100%, where the water vapor pressure is equal to the maximum amount of water vapor that the air can hold (saturation). Therefore, the difference of the measured temperature with the dew point is an indication of relative humidity. The frost point is the temperature at which water vapor begins to condense into solid form. Dew and frost points are functions of air pressure.

As mentioned above, humidity sensors are used in multiple fields and depending on the needs of each application, different types of sensors have been developed. The two main categories are Absolute Humidity sensors (Hygrometers) and Relative humidity sensors. The former are used for humidity detection purposes as primary sensors and detect the change in the amount of water vapor at a microscopic level. The latter are more widespread and constitute the majority of sensors used today as

their mechanism is simpler, their manufacture is cheaper and they are applied to the needs of everyday life. In general, the most widely used materials for relative humidity sensors are ceramics and semiconductors due to their mechanical strength, thermal resistance and stable responsivity, but other materials have been used like organic polymers and hybrids of organic and inorganic compounds (polymer in combination with ceramic material). These sensors can be further distinguished according to their principle of operation into resistive, capacitive, optical sensors etc.

2.1.2 Mechanisms of relative humidity detection

Grotthuss mechanism

By applying an electric potential difference to the device, mobilization of carriers is observed, specifically conductivity due to hydrogen ions (protons) between the water layers that have been formed. It is assumed that either due to collisions with the surface or due to the phenomenon of self-ionization of water molecules, hydrogen and hydroxyl ions are formed according to the following reaction:

$$H_2O \leftrightarrow H^+ + OH^-$$

At low levels of relative humidity, the surface of the sensing material is partially covered with water molecules, and the main carrier is the hydrogen ions H^+, which diffuse by hopping to the neighboring hydroxyl ions OH^- as shown in the figure below:

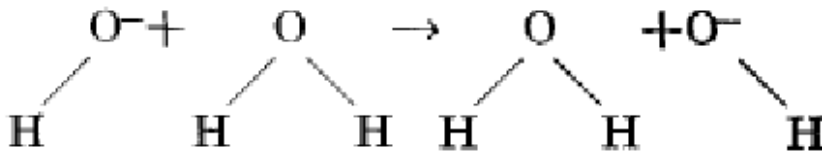

Figure 2: Grotthuss mechanism for hydroxyl ions. Reprinted.[1]

This mechanism is called the Grotthuss mechanism for hydroxyl ions.

In general, the Grotthuss mechanism is considered to be the main reason for the change of electrical conductivity as the relative humidity changes. This mechanism was first proposed by Theodor von Grotthuss in 1806 studying the electrolysis of water and the movement of positive ions.

1 Hamid Farahani, Rahman Wagiran, and Mohd Nizar Hamidon, "Humidity Sensors Principle, Mechanism, and Fabrication Technologies: A Comprehensive Review," *Sensors* 14, no. 5 (May 2014): 7881–7939, https://doi.org/10.3390/s140507881.

At higher values of relative humidity, a continuous layer of water is created on the surface of the material and the following reaction takes place:

$$H_2O + H_2O \leftrightarrow H_3O^+ + OH^-$$

therefore protons are channeled from one water molecule through the quantum tunneling effect to the next forming hydrogen bonds, as shown in the following figure:

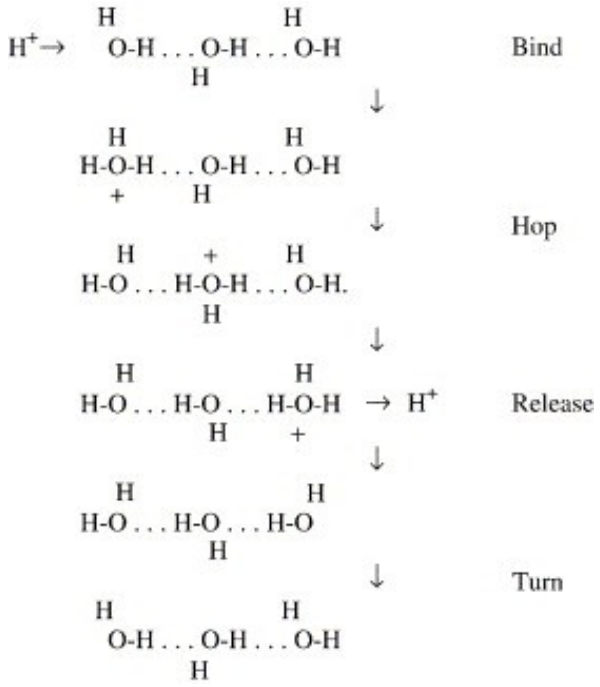

Figure 3: Diffusion of protons between water molecules. Reprinted.[2]

The more water layers are formed, the easier it is to produce hydronium H_3O^+. Thus, as the value of the relative humidity increases, the dominant carrier diffusion mechanism is that of protons between water molecules, and also the transfer of protons between hydroxyl groups.

Electron Doping

Another mechanism that has been proposed for humidity sensing is based on the change of conductivity as a result of a change in the Fermi energy level of ceramic semiconductors. It has been observed that as water molecules adsorb on the surface of a ceramic semiconductor (e.g. ceramic

2 Colin A. Wraight, "Chance and Design—Proton Transfer in Water, Channels and Bioenergetic Proteins," *Biochimica et Biophysica Acta (BBA) - Bioenergetics*, Proton Transfer Reactions in Biological Systems, 1757, no. 8 (August 1, 2006): 886–912, https://doi.org/10.1016/j.bbabio.2006.06.017.

oxides SnO_2, ZnO and others), they increase the conductivity of n-type semiconductors and correspondingly decrease the conductivity of p-type semiconductors.

There are two possible mechanisms involved in this process. In one of those, as water molecules are adsorbed, they donate electrons to the material, therefore doping it. In the other, water molecules replace previously adsorbed oxygen ions (O^-, O^{2-}, etc.) and thus electrons are released into the material. Therefore both processes can result in electron doping of the material and change the Fermi energy.

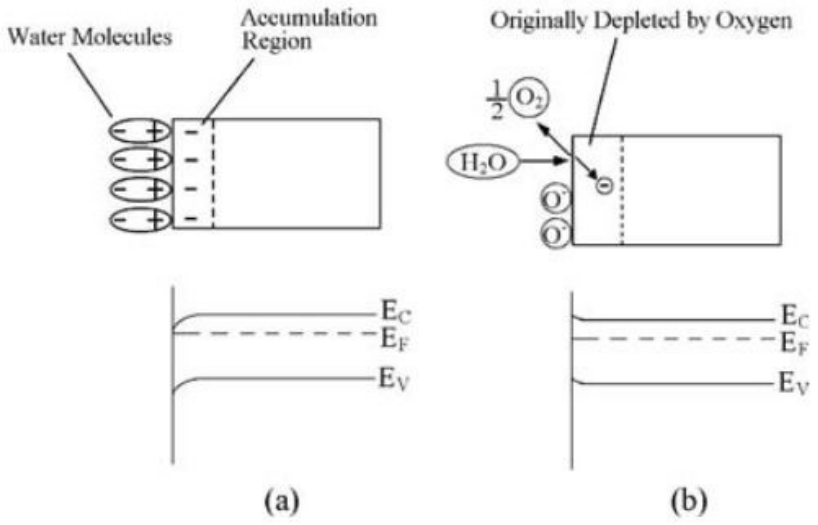

Figure 4: (a) Adsorption of water molecules and electron doping, (b) Replacement of previously adsorbed oxygen ions and electron doping. Reprinted.[3]

As the relative humidity increases and a layer of water is created on the surface of the detection material, an increase in conductivity due to hydrogen ions is observed as mentioned above. Therefore, at room temperatures the conductivity of semiconductors is due to both proton and electron mobility. However, at higher temperatures (> 100 °C), water molecules cannot condense so the main mechanism of conductivity change should be attributed to electron doping of the semiconductor.[9]

2.1.3 State of the art of relative humidity sensors based on 2D materials

Currently, commercial electrolytic humidity sensors in use are characterized by low relative humidity ranges and response times in the range of ~30 to ~60 s. Research has focused on fabricating sensors with high sensitivity at a wide humidity range, quick response and recovery time, repeatability, inexpensive large scale fabrication, and low power consumption. As mentioned previously, two-

3 Zhi Chen and Linge Xiao, "Humidity Sensors: A Review of Materials and Mechanisms," *Sensor Letters* 3 (December 1, 2005), https://doi.org/10.1166/sl.2005.045.

dimensional materials have been widely studied for sensing applications, because of their high surface to volume ratio, which supports all the parameters mentioned above. A lot of work has been produced regarding the application of two-dimensional materials as relative humidity sensors. The most famous two-dimensional material, graphene, is not a great candidate for this application, due to its band gap being equal to zero, which neutralizes the above mentioned doping-based sensing mechanisms. However a lot of work has been published for graphene oxide GO and transition metal dichalcogenides TMDs. The sensitivity, response and recovery times vary, and the selectivity is a topic under discussion. As reported by Jenjeti R. N. et al (2019)[10], $NiPS_3$ is a great candidate as a humidity sensing material, exhibiting exceptional sensitivity with a value of $\sim 10^6$, state-of-the-art response and recovery times, and extremely high selectivity.

Table 1: State of the art: Relative humidity sensors base on two dimensional materials

Material	***Sensitivity***	***RH Range***	***Response Time***	***Recovery Time***
MoS2/Pt[11]	4000	35-85%	91.2 s	153.6 s
WS2/Au[12]	$7 \cdot 10^4$ at 75%	25-75%	107 s	13 s
ReS2[13]	18.26	43-95%	142.94 s	35.45 s
TaS2[14]	201.9 to 0.4	11-95%	0.6 s	2.0 s
MnPS3[15]	70650	0-100%	1-2 s	4 s
NiPS3[10]	$\sim 10^6$	0-100%	1-2 s	3 s

Although a lot of work has been produced on the topic of two-dimensional materials and humidity sensors, there is no connection between the structural characteristics resulted from the chosen fabrication parameters and the electrical characteristics. Furthermore, a lot of scientific papers exhibit results from electrical impedance spectroscopy, but the quality of the results is limited by problems arising due to the complexity and difficulty in developing a high precision and full controllable EIS set-up with a wide range of frequencies.

2.2 Two dimensional materials

2.2.1 General

A two-dimensional material is a crystalline material which exhibits strong bonds in plane and has a closed chemical structure. These layers are joined by Van der Waals bonds between them and form a multi-layer material.

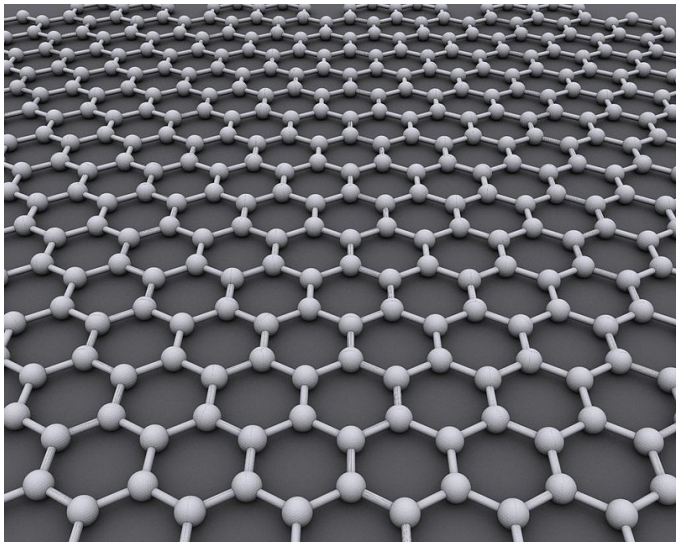

Figure 5: Graphene. Reprinted.[4]

In the past it was believed that two-dimensional structures are not thermally stable. But in 2004, Andre Geim and Konstantin Novoselov at the University of Manchester managed to isolate and characterize graphene for the first time[16] and were awarded the Nobel Prize in 2010 for pioneering experiments on this two-dimensional material. Scientists have succeeded in extracting single-atom-thick layers (graphene) from the well-known multi-layer material, graphite, by the mechanical exfoliation technique (repeated peeling) using adhesive tape.

Despite its excellent properties such as high thermal and electrical conductivity, high absorption of the entire optical spectrum, mechanical strength and elasticity, is not suitable for many applications. Its band gap is equal to zero so it cannot, for example, be used in MOSFETs due to the low on/off ratio of the device. Thus, in recent years, other families of two-dimensional materials have been explored, such as transition metal dichalcogenides (TMDs) MX_2, hexagonal Boron Nitride (h-BN) and of course transition metal phosphorus trichalcogenides MPX_3.

4*https://en.wikipedia.org/wiki/Graphene*

The last few decades semiconductor industry following Moore's law, which states that the number of transistors in an integrated circuit (IC) doubles about every two years. Currently state of the art CMOS technology has reached a channel length of 5nm. Further scaling of the channel also requires reducing its thickness to suppress short channel effects. For three dimensional materials like Si this can lead to (charge scattering at the interfaces) due to surface states and results in a dramatic drop of the carrier mobility, thus ruining device performance. Two-dimensional materials, on the contrary, present inherent advantage due to quantum confinement in two dimensions, so the mobility remains high even at the atomic thickness limit. They are important candidates for gas, chemical and biosensing, because of their high surface-to-volume ratio and versatile functionalization. As even single charged particles and molecules can drastically modify the conductivity, such 2D layered structures exhibit very high sensitivity to doping. So, precise fabrication and functionalization process is key to incorporating two-dimensional materials in modern electronics. Manufacturing processes for of these materials are still in need of further research, as defects and contamination are not yet compliant with specification defined for production. [17]

2.2.2 Fabrication of two dimensional materials

2D materials can be produced using several methods, those can be categorized in two big groups: bottom-up synthesis and top-down exfoliation. In the first case, a chemical reaction of organic compounds and other molecules is taking place on a suitable substrate at a controlled temperature. Such methods are chemical vapor deposition (CVD) or plasma-enhanced chemical vapor deposition (PECVD) and molecular beam epitaxy (MBE). In the latter case, exfoliation of the original multi-layer crystal is performed by methods such as mechanical exfoliation (adhesive tape), chemically using ultrasonication, laser assisted or microwave assisted exfoliation, and others.

Ultrasonication typically generates a high frequency ultrasound at a desired power value and it is applied to a solution containing the material. Sound waves result in the creation of pressure cycles in the liquid with alternations from high pressure (compression) to low pressure (rarefaction) and the formation of void in the liquid which collapses violently locally creating high temperatures (cavitation). The goal is to separate the layers of two-dimensional materials which are connected to each other by Van der Waals forces and homogenize the solution. Two devices are used for this procedure: the ultrasonic probe sonicator and the ultrasonic bath.

Figure 6: Probe sonicator. Reprinted.[5]

The ultrasonic probe consists of a generator which converts the alternating current into a signal of a certain frequency (e.g. 20 kHz), which then ends up modulating in a piezoelectric transducer. The transducer converts the electrical signal into a mechanical vibration, which then is transferred to the tip of the probe. The probe is usually made of titanium alloys and its diameter is chosen according to the amount of the sample to be processed. Smaller diameters provide high-intensity ultrasound, but the energy is focused on a smaller area, whereas larger tip diameters can treat larger volumes. The tip longitudinally expands and contracts, and the distance it travels is proportional to the amplitude of the applied power chosen by the user. The pressure cycles formed by this process result in the exfoliation of the 2D material.

5*https://adelab.com.au/ultrasonic/qsonica-q125-sonicator-ultrasonic-cell-disrupter*

Figure 7: Bath sonicator. Reprinted.[6]

The principle of operation of the ultrasonic bath is similar to that of the probe, with the difference that the mechanical vibrations produced by the piezoelectric material is not transferred to a probe, but to a water bath in which the sample is placed. Ultrasonic baths are much more economical than probes, and are generally preferred for homogenization and stirring of the sample, while the probes offer power in a more concentrated area, and are therefore preferred for exfoliation.

2.2.3 $NiPS_3$

$NiPS_3$ is a two-dimensional material, which belongs to the family of MPX_3 (Transition Metal Phosphorus Trichalcogenides). The structure of the material comprises a plane of Ni atoms arranged in a honeycomb pattern and are octahedrally coordinated by six sulfur atoms S. The S atoms are connected to two P atoms located above and below the primal plane. Two P atoms and six S atoms are covalently bonded among themselves, forming a $(P_2S_6)^{4-}$ anion complex of a pyramidal structure. The crystal structure of bulk NiPS3 shows monoclinic symmetry, exhibited by the AB stalking of the atomic layers along the c axis.

6*https://www.indiamart.com/proddetail/bath-sonicator-9244177612.html*

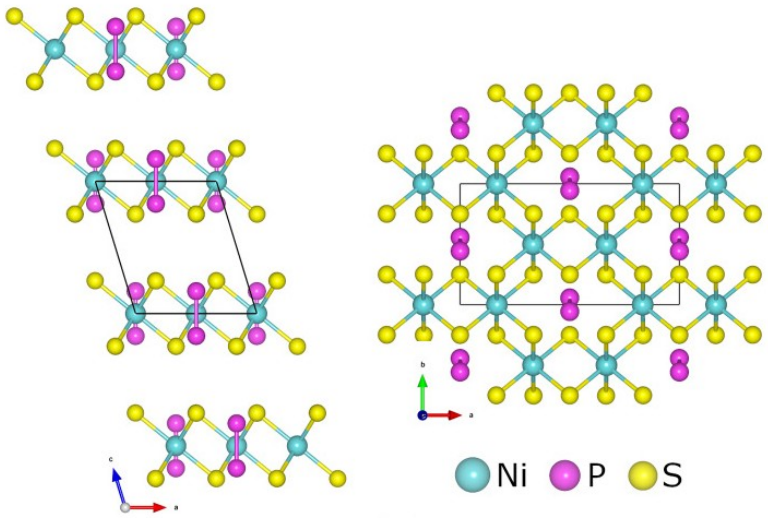

Figure 8: Monoclinic crystal structure of $NiPS_3$. Reprinted[7]

Table 2: Key characteristics of Graphene, MoS_2, $NiPS_3$

	Graphene	***MoS_2***	***$NiPS_3$***
Interlayer gap	3.4 Å	6.5 Å	6.7 Å
Single layer thickness	~0.34 nm	~0.65 nm	~0.67 nm
Single layer band gap	0 eV	~1.9 eV	~1.6 eV

Several attempts have been made to fabricate different electronic structures using the novel 2D material, Jenjeti R. N. et al (2018) fabricated a field effect transistor based on layered $NiPS_3$ characteristics showing n-type behavior with on/off ratio of 10^3–10^5[18], and Chu et al. (2017) present high performance ultraviolet photodetector based on few-layered 2D $NiPS_3$, outperforming some traditional wide-bandgap UV detectors[19]. It is important to be mentioned that Latiff et al. published a paper on cytotoxicity of layered metal phosphorus chalcogenides, in which it was found that $CoPS_3$ was the most toxic, followed by $FePS_3$ with intermediate toxicity, while $NiPS_3$ showed the lowest toxicity among the three materials tested. When viewed with other layered materials, these MPS_3 samples present comparable toxicities with transition metal dichalcogenides and black phosphorus at low concentrations. [20]

7 Lane and Zhu, Thickness Dependence of Electronic Structure and Optical Properties of a Correlated van Der Waals Antiferromagnetic NiPS_3 Thin Film.

2.3 Electrical impedance spectroscopy

Electrical impedance spectroscopy is a complex process by which conclusions can be drawn about the electrical behavior of a system -a device- by measuring its impedance over a range of frequencies. Impedance is a complex number that expresses the resistance of the circuit to the movement of electrons and includes contributions from resistors, capacitors and inductors. Impedance is measured by applying an alternating voltage of a certain frequency to the circuit and measuring the alternating current accordingly. In general, electrochemical systems do not exhibit linear behavior and for this reason it is important that the applied signal is small so that there is no production of harmonics.

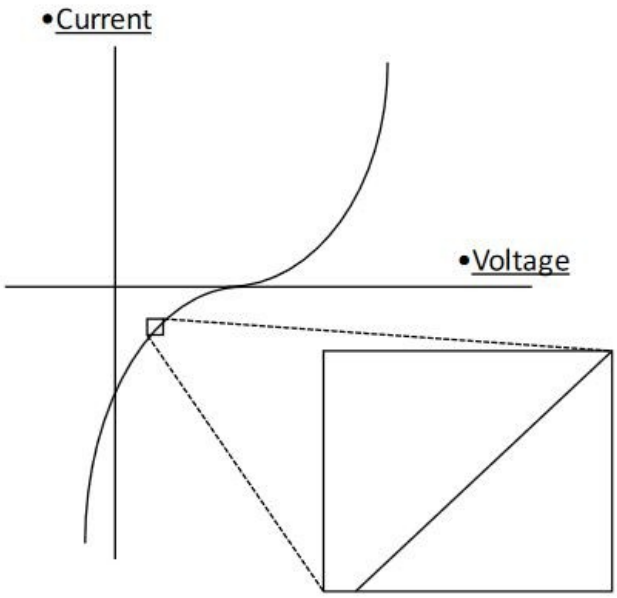

Figure 9: Linear approximation for electrochemical systems

In systems that can be considered approximately linear, the response of the current to a sinusoidal alternating voltage is also a sinusoidal of the same frequency but shifted by a phase difference φ.

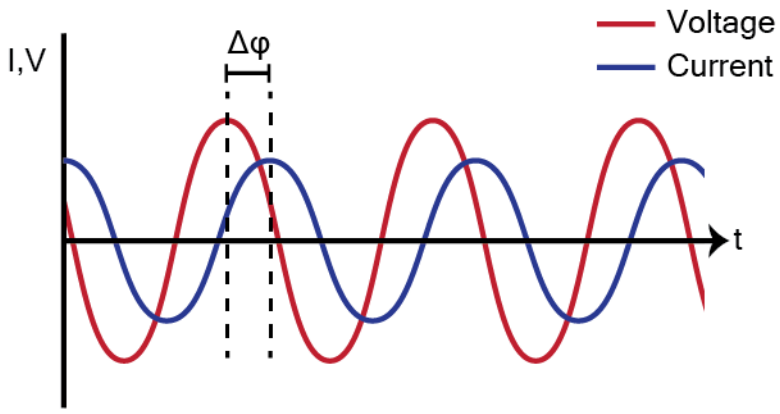

Figure 10: Phase difference. Reprinted.[8]

The applied voltage is of the form:

$$V_t = V_0 e^{\omega t} \quad \mu\varepsilon \quad \omega = 2\pi f$$

and the current response:

$$I_t = I_0 e^{\omega t + \varphi}$$

And therefore the impedance arises:

$$Z = \frac{V_t}{I_t} = \frac{V_0 e^{\omega t}}{I_0 e^{\omega t + \varphi}} = Z_0 e^{\omega t + \Delta\varphi}$$

Therefore the impedance is characterized by its magnitude Z_0 and the phase difference φ.

To understand the data obtained by electrical impedance spectroscopy of an electrochemical system, it is useful to create an equivalent electrical circuit. The most common elements used are the resistor, capacitor and inductor depending on the phase difference observed.

8*https://www.gamry.com/application-notes/EIS/basics-of-electrochemical-impedance-spectroscopy/*

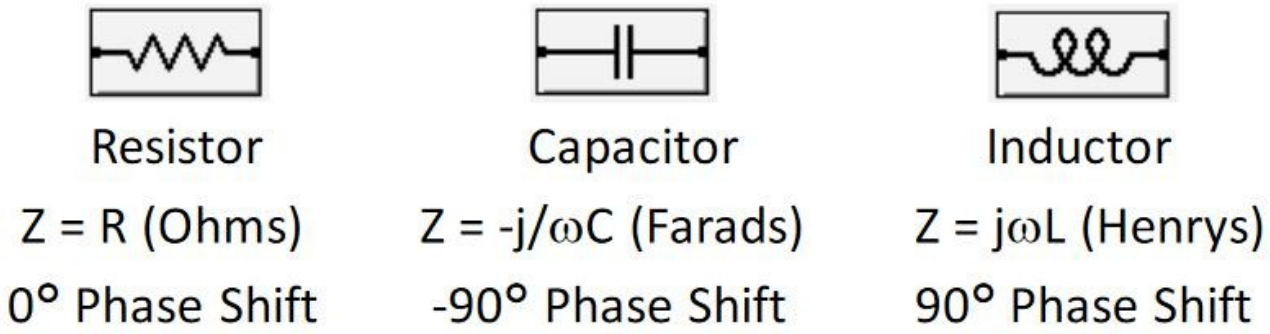

Figure 11: Passive elements of a circuit. Reprinted.[9]

The impedance of an ideal resistor is independent of frequency, therefore, it has no imaginary part. Conversely, the impedance of an ideal capacitor and an ideal inductor only have an imaginary part, their magnitudes depend on the frequency, and the current is out of phase with the applied voltage by -90° and +90° respectively.

The most common equivalent electrical circuit created in electrochemical systems is the simplified Randles cell.

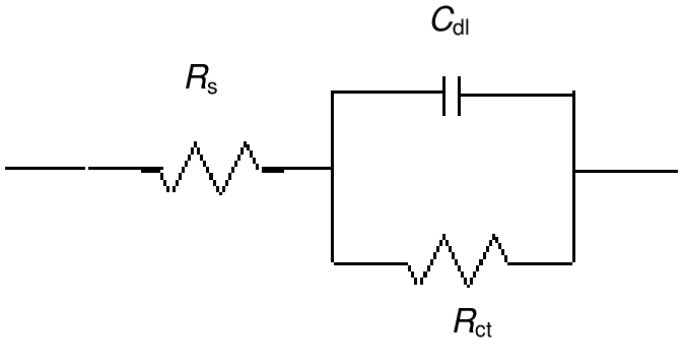

Figure 12: Randles cell. Reprinted.[10]

The simplified Randles circuit consists of a resistor R_1 in series with a capacitor C connected in parallel with a second resistor R_2. At high frequencies, the capacitor acts as a short circuit, so the current passes

9*https://www.gamry.com/assets/Uploads/BasicsOfEIS.pdf*

10*Rosliza, R.. (2012). Improvement of Corrosion Resistance of Aluminium Alloy by Natural Products. 10.5772/32952.*

almost entirely through it. On the contrary, at low frequencies it works as an open switch, so the current passes through the R_2. This behavior can be graphically represented in two ways. The Nyquist plot (left in fig. 13) and the Bode plot (right in fig. 13).

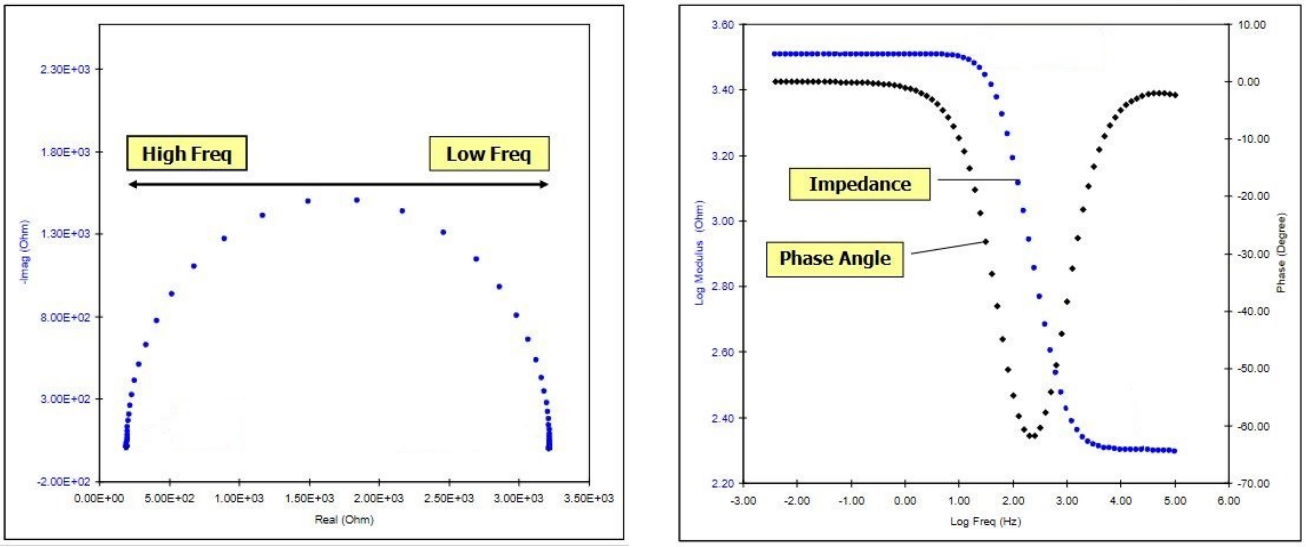

Figure 13: Nyquist and Bode diagrams. Reprinted.[11]

In the Nyquist diagram it is clear that at high frequencies, when the capacitor acts as a short circuit, the value of the impedance has zero imaginary part, therefore the diagram gives the value of the ohmic resistance R_1. Since at low frequencies the capacitor acts as an open switch, the diagram also gives an actual value of the sum of the resistors R_1 and R_2. The values of these resistances are also visible in the Bode diagram from the impedance intensity axis. However, the second curve of the diagram is also very important, as it gives the phase difference introduced by the system for each frequency. At high and low frequencies, when the phase difference is zero, the system has an ohmic resistance behavior, while it varies in between due to the capacitor.

Another element used in electrochemical circuits is the Warburg element and represents resistance to mass transfer. It is a generalized impedance element that controls the dissipation in the system and introduces a phase difference of 45°. This item causes a change in the above diagrams as presented in fig. 14.

11 https://www.gamry.com/assets/Uploads/BasicsOfEIS.pdf

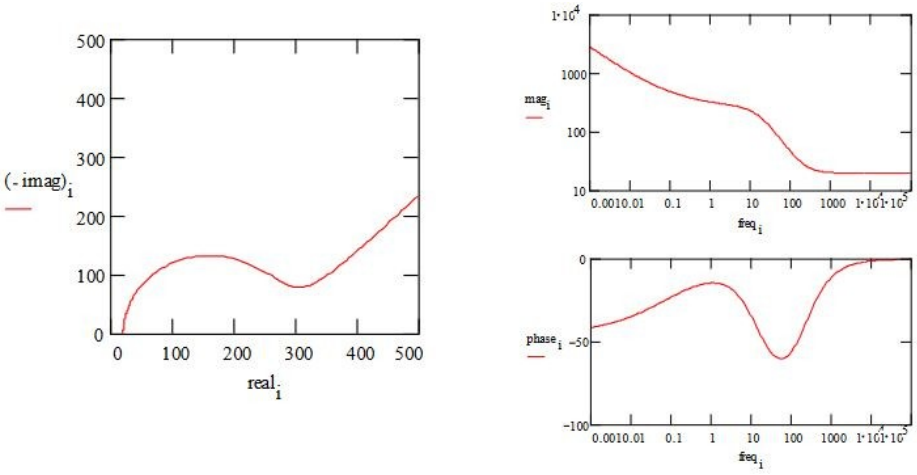

Figure 14: Nyquist and Bode diagrams includin Warburg element. Reprinted.[12]

The effect of this element is observed at low frequencies. In the Nyquist diagram, it is clear that at low frequencies, instead of returning to zero imaginary resistance, the curve changes direction and creates a straight line at an angle of 45°. As in the Bode diagram, the straight line that was previously created at low frequencies is now inclined.

Since diffusion effects are observed at low frequencies, the resulting equivalent circuit is presented in fig.15.

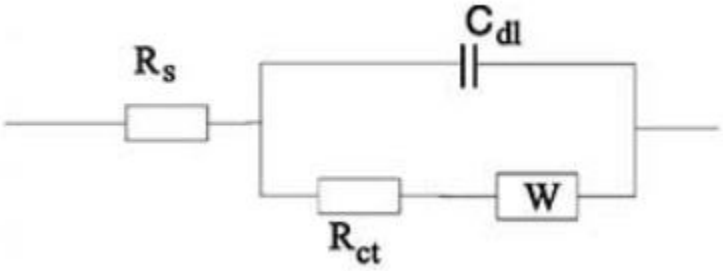

Figure 15: Equivalent Randles cell including Warburg element. Reprinted.[13]

12*https://www.gamry.com/assets/Uploads/BasicsOfEIS.pdf*

13*https://www.gamry.com/application-notes/EIS/basics-of-electrochemical-impedance-spectroscopy/*

In general, the resistance placed in parallel with the capacitor seems to represent phenomena such as carrier movement and polarization effects, while the resistance in series, as the resistance that the device presents.

2.4 Fabrication of the sensors

2.4.1 Photolithography

Lithography is a method used in the field of microelectronics to build patterns in small dimensions. Two techniques that are mainly used are photolithography and electron beam lithography. Depending on the requirements of the layout, the appropriate method is chosen. Photolithography is simpler to perform, and can produce devices down to a few tens of nanometers, while electron beam lithography is up to an order of magnitude smaller with excellent precision, but the cost is much higher. The process of photolithography or lithography-UV is based on the exposure of a photosensitive material, resist, to ultraviolet light in order to create the desired patterns. In more detail, to carry out the process, the substrate must first be chemically prepared, cleaning it using the RCA method and exposing it to oxygen plasma so that the surface gets hydrophilic behavior, and then the chemical HMDS (hexamethyldisilazane) must be deposited. HMDS is a hydrophobic substance that is used to prevent the aqueous developer from entering between the resist and the substrate, which have the unwanted result of lifting the resist and eroding the printed pattern. Then, after the HMDS is activated using a hot plate, and subsequently the resist is placed. The resist can be either positive or negative depending on the optical mask to be used.

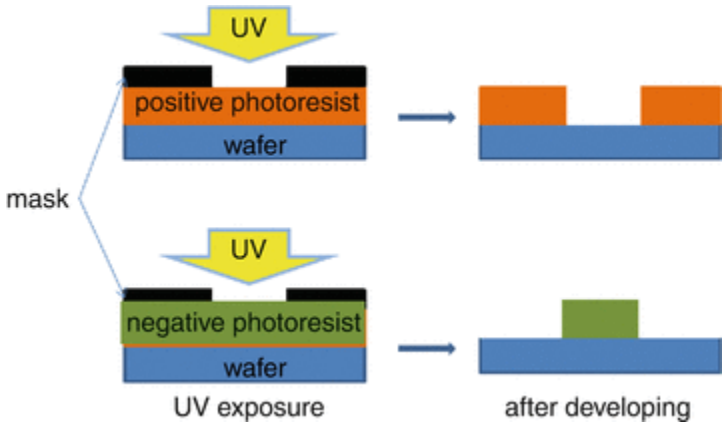

Figure 16: Photolithography. *Reprinted.*[14]

14*https://media.springernature.com/original/springer-static/image/prt%3A978-90-481-9751-4%2F16/MediaObjects/978-90-481-9751-4_16_Part_Fig1-342_HTML.gif*

The positive resist, when exposed to UV light becomes soluble to the developer, and therefore when the developer is applied, the areas that have been exposed to UV light is removed. On the contrary, the negative resist becomes insoluble, and therefore when the developer is applied, the areas that have not been exposed to UV light are removed. Finally, after the stabilization of the resist using hot plate, the developer is applied to develop the final pattern.

2.4.2 Electron-beam physical vapor deposition

Electron beam metal physical vapor deposition is a method by which thin films and coatings of materials can be fabricated in vacuum using an electron beam as a heat source.

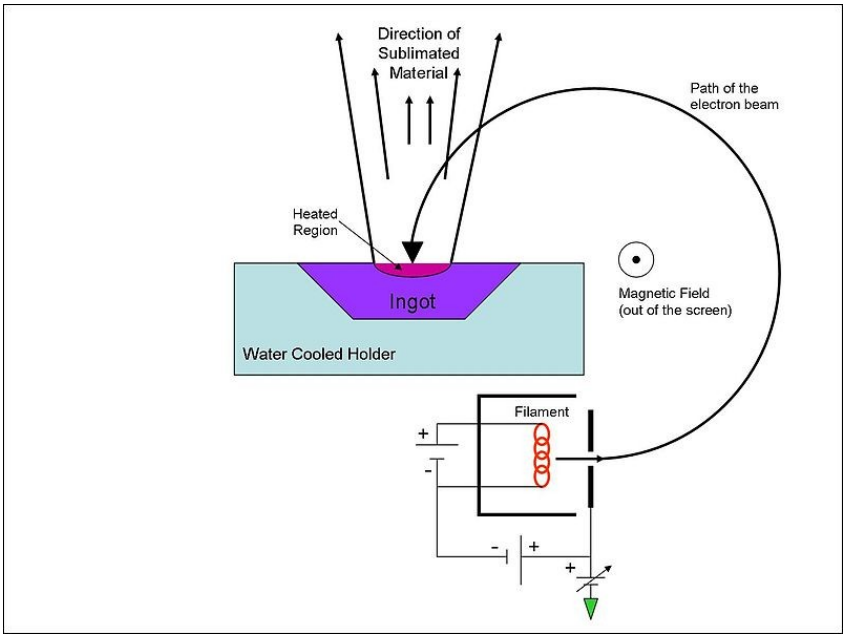

Figure 17: Electron beam metal physical vapor deposition. *Reprinted.*[15]

In this method an electric potential is applied to a filament, usually made of tungsten, which leads to Joule heating and thermal emission of electrons. The electrons, which are accelerated with a high applied voltage, are focused by a strong magnetic field on the container containing the material. It is important that a vacuum of at least 7 x 10^{-5} Torr is created to allow electrons to pass from the electron source to the material container and the evaporated material to reach the target without stopping at air molecules. The values of the potential that accelerates the electrons can be from 3 to 40 kV which results to the current of the electron beam being a few Amperes. Upon impact with the material, a percentage of the kinetic energy of the electrons (~85%) is converted into thermal energy and this

15*https://en.wikipedia.org/wiki/Electron-beam_physical_vapor_deposition*

causes heating and eventually evaporation or sublimation. The remaining percentage of the kinetic energy of the electron beam is consumed either in the production of X-rays or in the production of secondary electrons. Therefore, if there are sufficient levels of vacuum and temperature, a vapor of the material receiving the electron beam will be created and thus coatings are deposited on the sample. The thickness of the coating at any time is measured with a quartz crystal which has been set in oscillation, and due to the increase in its mass by the material coating, the frequency of oscillation is reduced. In this way, the mass per unit area is precisely measured and, taking into account specific parameters of the material, the coated thickness can be calculated.

2.4.3 Deposition

Dip coating

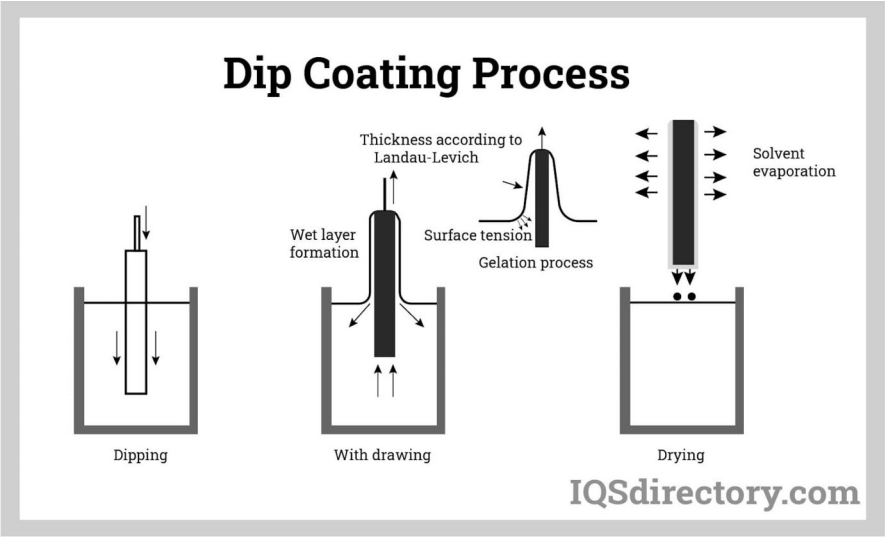

Figure 18: Dip coating process schematic. Reprinted.[16]

Dip coating is a process widely used in research in order to create a thin uniform film on a substrate. The process includes immersion of the substrate into the solution and withdrawing it at a constant speed to avoid any jitters. The thickness created is according to Landau – Levish problem in fluid dynamics, which assumes that the plate is dragged out of the liquid slowly, so that the three major forces which are in balance are the viscous force, the force due to gravity, and the force due to surface tension. Dip coating is widely used in industry, as it is a straightforward, inexpensive, and easily repeatable process for large volume projects.

16 https://www.dipmoldedplastics.com/dip-coating/

Spin coating

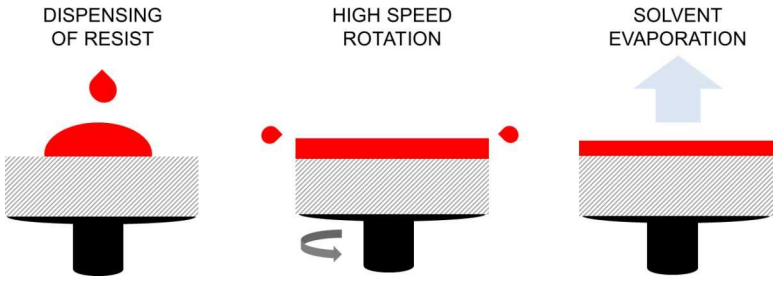

Figure 19: Spin coating process schematic. Reprinted.[17]

Spin coating is another process used for the fabrication of thin films on a substrate. The process involves the application of a small amount of the solution on the center of a substrate, and then rotating it at speeds up to 10,000 rpm to spread the material uniformly. The operating principle is based on the centrifugal force and the thickness of the coating depends on the angular speed, the viscosity and concentration of the solution. Spin coating is also a widely used method in industry due to its high control over the produced thickness of the film and the simplicity of the process.

3 Experimental

3.1 Electrical impedance spectroscopy set up

3.1.1 Hardware

One option for performing EIS relies on applying a single stimulus formed by multiple frequencies, and performing a simultaneous analysis through a fast Fourier transform algorithm. However, this approach is computationally expensive, highly sensitive to noise, and its complicated signal processing hardware implies big costs. As a result, commercial spectrometers deal with one frequency at a time.The most common set-up for impedance spectroscopy is potentiostatic (or galvanostatic) EIS. This method is performed at a fixed DC potential with sinusoidal potential perturbation superimposed and applied to the cell. In the potentiostatic or galvanostatic modes, the resulting current or potential respectively is measured to determine the impedance of the system. Potentiostatic/ galvanostatic commercial impedance analyzers are available in the industry, but the frequency range is constrained by the instrument limitations, since control over the averaging and time constant is poor, and the amplitude of impedance measurement is highly restricted (>1kΩ). Several solutions have been suggested for the improvement of various parameters, such as implementing an external oscillator to achieve a wider frequency range, or using op-amps for lower impedances (>100Ω), but there are still several

17 https://www.inseto.co.uk/what-is-spin-coating-ikb-075/

limitations. Another option that has been proposed regarding the impedance read-out circuit, is the lock-in approach.[22]

The set up designed is pictured in Fig. 20:

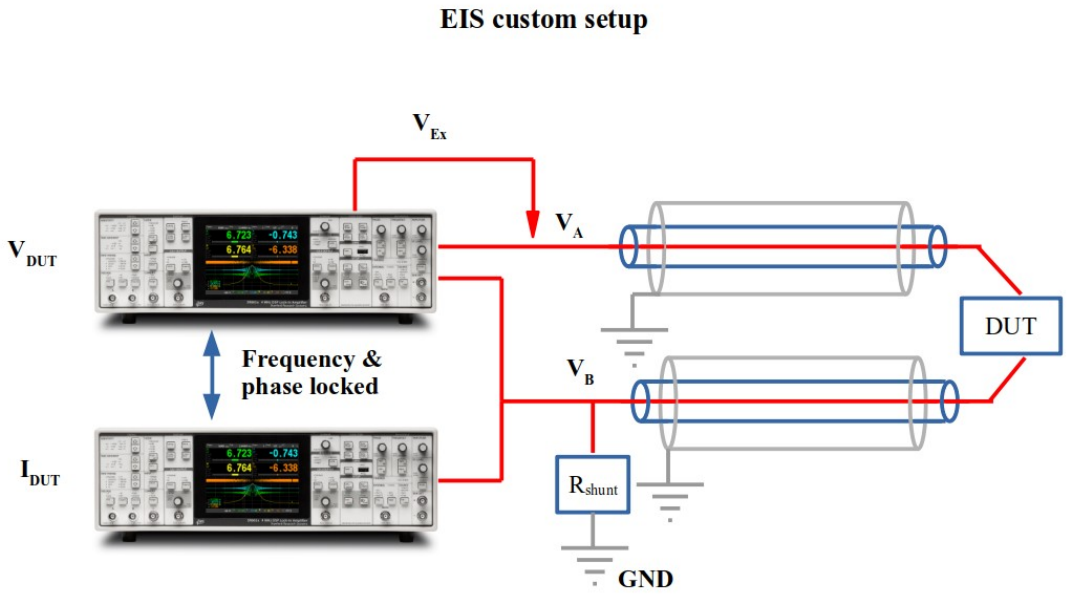

Figure 20: Electrical impedance spectroscopy custom set up

We are using two lock-in amplifiers from Stanford Research Systems, SR865A, 4 MHz DSP. They are connected to each other so they are frequency and phase locked. The master lock-in, depicted on the upper part of fig. 20, generates the excitation signal of the system and measures the voltage difference (amplitude and phase) on the device. The slave lock-in, shown below the master lock-in in fig. 20, measures the voltage difference on a shunt resistance, so it can calculate accurately the current (amplitude and phase), going through the device. Therefore using a home-made software described in the next section (3.1.2), we can automate the measurement of the complex impedance of the DUT for any frequency spectrum between 1 mHz and 4 MHz. Finally, triaxial cables and op-amps are used in order to shield the inner transmission line carrying the signal and remove the parasitic capacitance, as shown in figures 21 and 22.

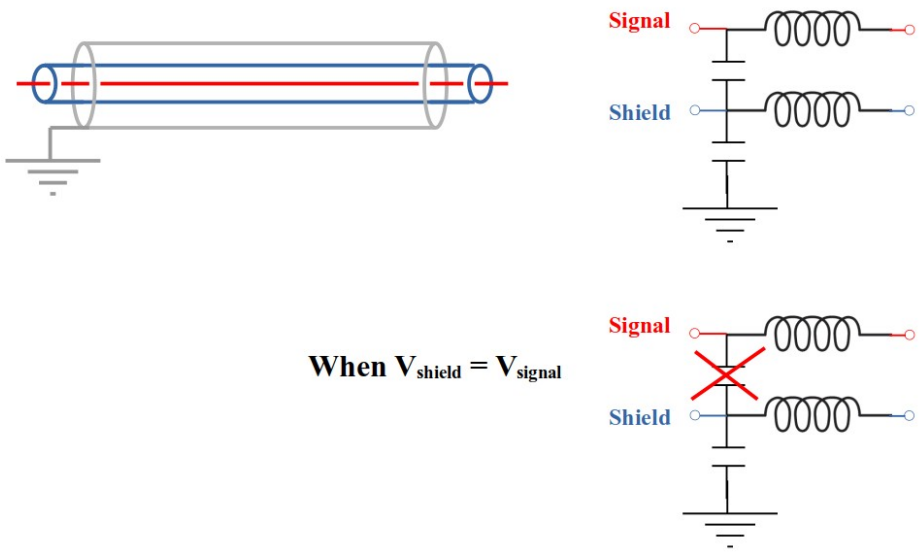

Figure 21: Removal of parasitic capacitance

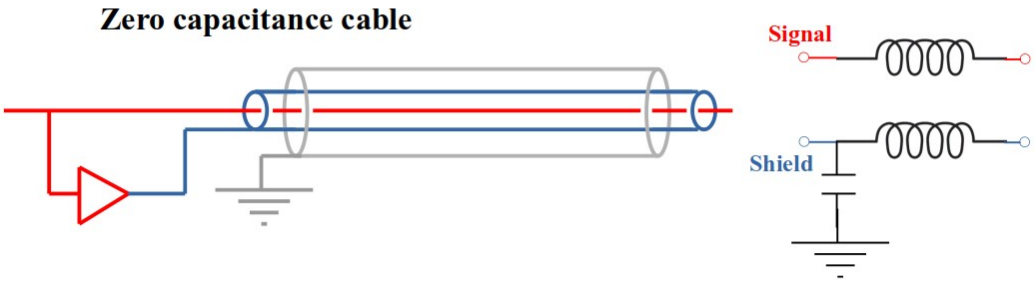

Figure 22: Triaxial cable and operational amplifier for zero capacitance cable

3.1.2 Software

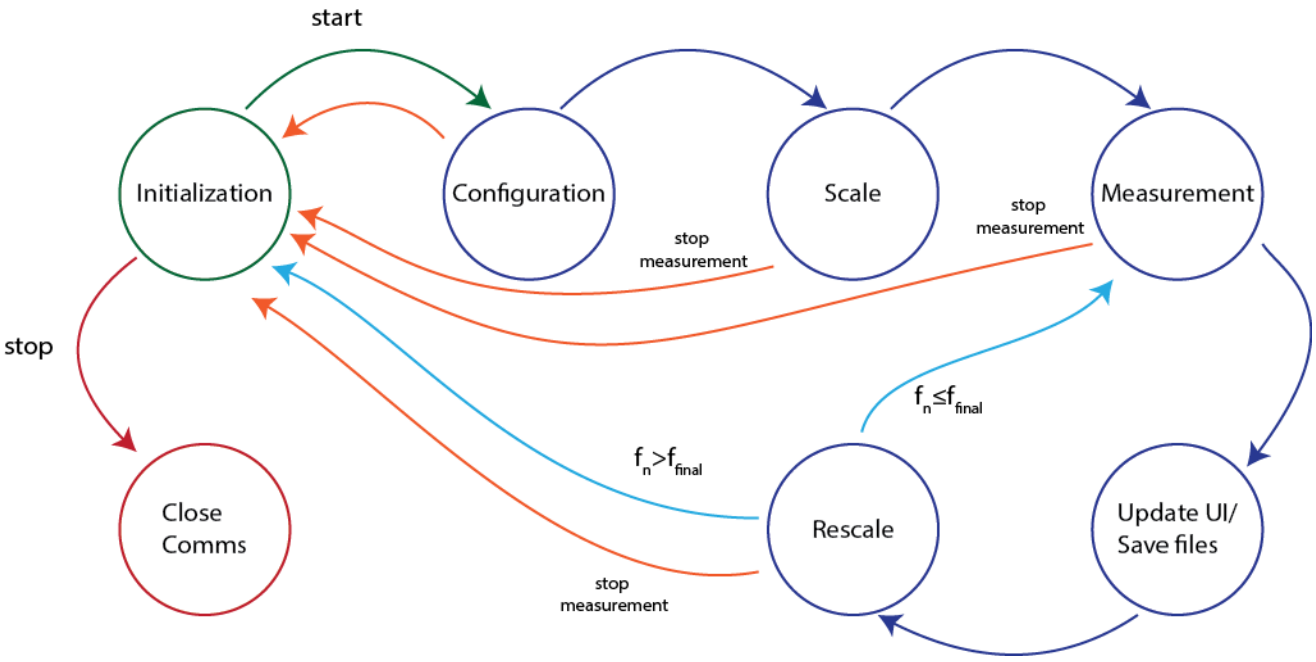

Figure 23: Finite state machine diagram

The software for the control of the set up is built using NI LabView. The program is built as a Finite State Machine (FSM) model, so it can transition from one state to another in response to some inputs. The diagram above is the FSM diagram describing the structure of the LabView program.

The initial state of the machine is the “Initialization”. In this state the user can select the parameters of the measurement such as the initial and final frequency, counts per decade, sine out amplitude, filter slope, and software and hardware averaging values. Once the start button is pressed, the EIS procedure begins.

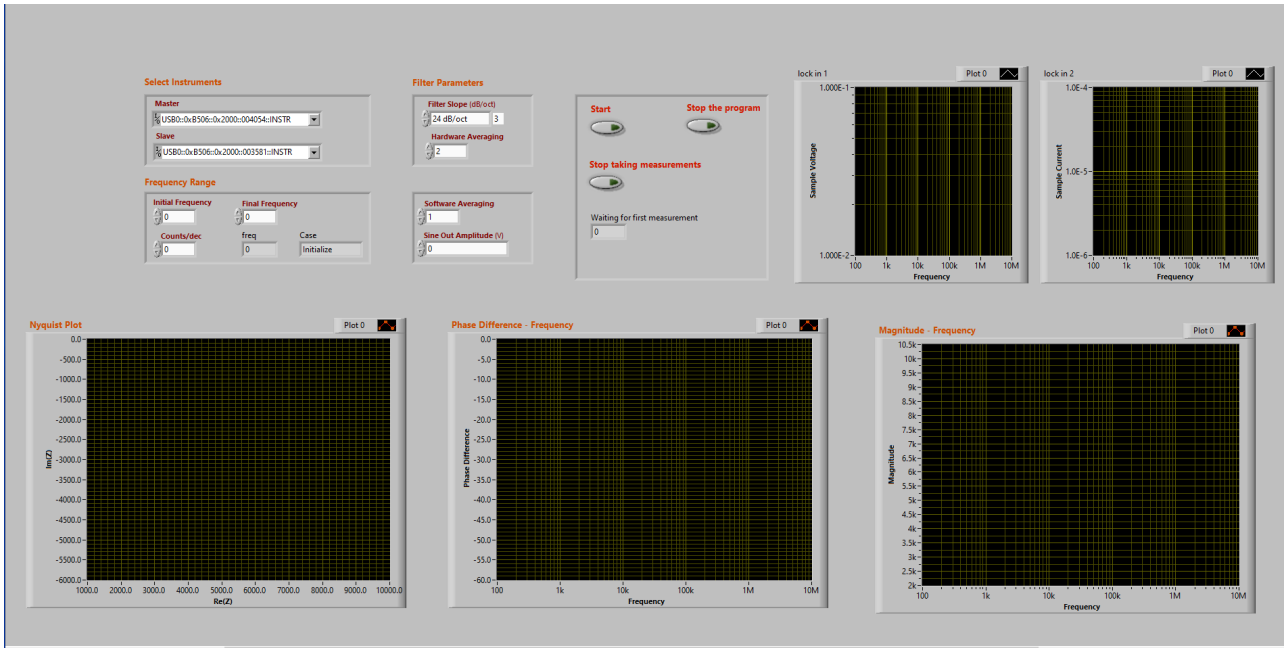

Figure 24: Front panel of LabView NI program for electrical impedance spectroscopy.

The next state is “Configuration”, in which the program instructs the lock-ins to initialize some parameters such as initial frequency, maximum voltage range, appropriate time constant as well as the amplitude of the output signal. Next is the “Scaling” state. In this state the program gets a mock measurement to rescale its settings and choose an appropriate voltage range, so the accuracy of the measurement for both lock-ins is optimal. Following is the “Measurements” state, in which the software averaging becomes possible and the final measurement passes to the next states, where the graphs and the measurement file are updating and a rescaling regarding the last measurement is instructed. From there, if the next frequency is smaller than the final frequency chosen by the user, the program will proceed to the “Measurements” state; on the contrary, if the next frequency is smaller than the final frequency, the program will return to the “Initialization” state. From there, the user can either proceed to the next measurement procedure, or terminate the communication with the lock-ins and stop running the program.

3.2 Humidity control set up

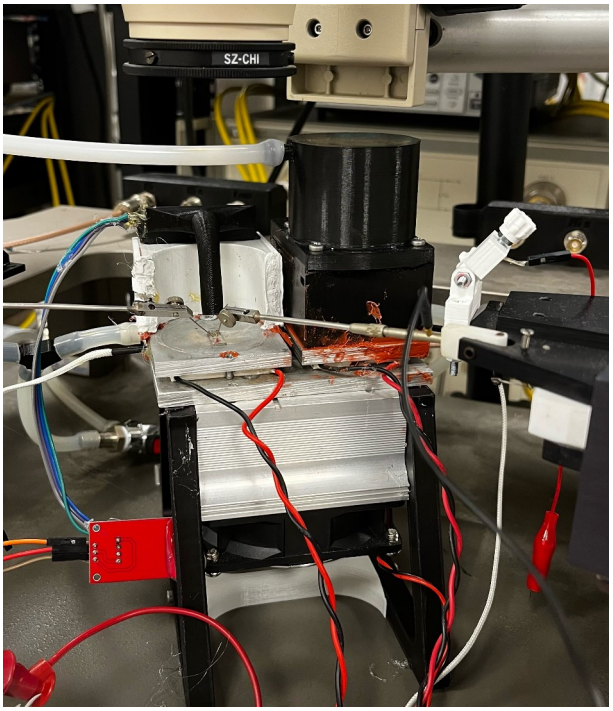

Figure 25: Humidity control set up

The custom humidity control set up consists of two separate parts. The right one is a sealed chamber containing water that is under a controlled temperature T_1. Dry air is entering from the bottom and exiting from the top resulting of saturated air at this particular temperature. Eventually, the air is focused on the sensor, which is kept at a controlled temperature $T_2 > T_1$, the absolute value of which is adjusted to achieve the desired relative humidity value. A schematic of the set-up is presented in fig. 26.

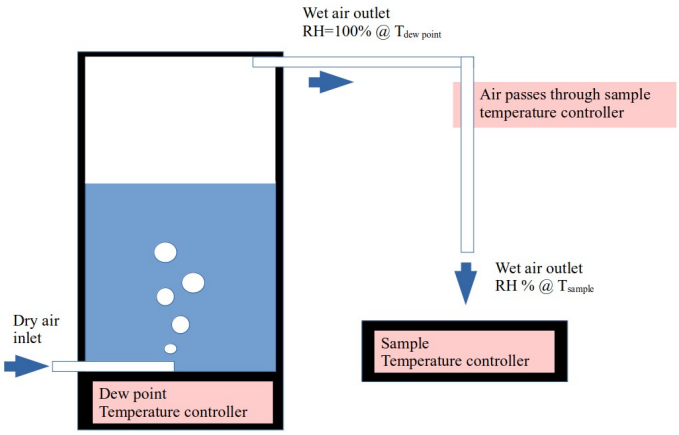

Figure 26: Humidity control set up schematic

3.3 Fabrication of the sensors

3.3.1 Liquid exfoliation on $NiPS_3$

The fabrication of $NiPS_3$ few layer flakes was performed using the liquid exfoliation technique and more specifically using a probe sonicator Qsonica Q125. The parameters chosen for the procedure are the chosen solvent, the applied power (which in this case is a percentage of the maximum power the sonicator can generate, aka 125 Watts), and the duration of ultrasonication. It is important for the sample to be kept in a bath of ice to avoid the evaporation of the solvent.

In previous work we showed how the selection of each of these parameters is crucial for the resulting flake size. As shown below the size of the flakes that had been exfoliated for a duration of 5 minutes is clearly larger than those of one hour. It is important to mention that after some time there is no particular difference in the observed flake size and they reach a threshold size, depending on the applied power. The reason behind that is that the chosen applied power corresponds to a particular acceleration of the probe sonicator and therefore the force that needs to be applied to the material in order to change its flake size is directly depended on its mass. Thus the mass will reach a threshold value, where the applied force is not sufficient to lead to further miniaturization of the flakes.

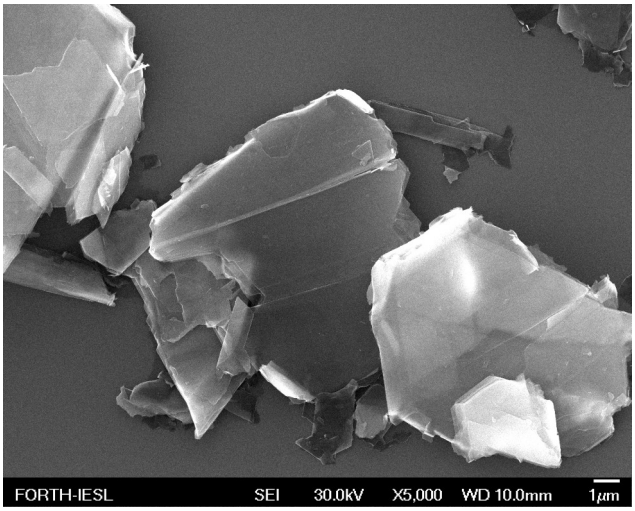

Figure 27: Chloroform – 60% applied power – Duration *5min – x5,000*

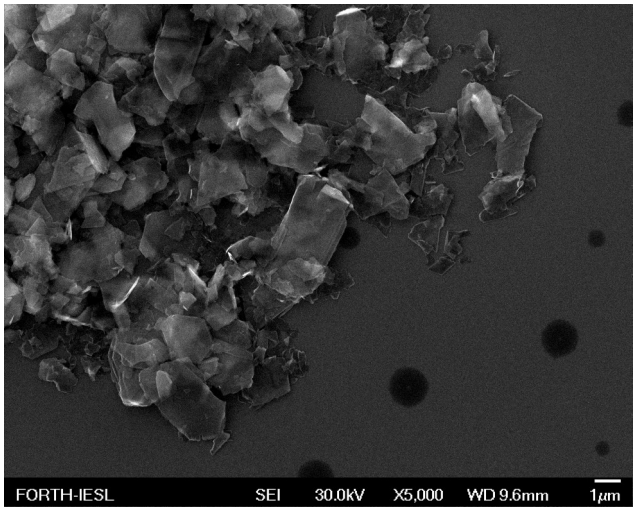

Figure 28: Chloroform – 60% applied power – Duration *60min – x5,000*

Also, flake size reduction is observed as the applied power increases. As the power increases, the acceleration of the tip of the probe sonicator increases and therefore more force is applied and the material will be able to break into smaller pieces.

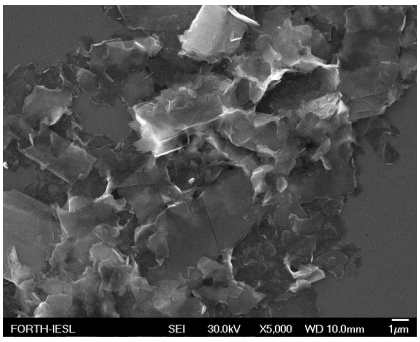

Figure 29: Chloroform – *20% applied power* – Duration *60min – x5,000*

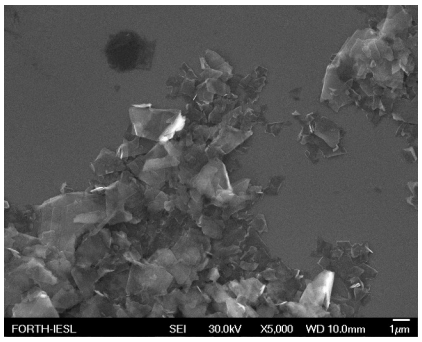

Figure 30: Chloroform – *40% applied power* – Duration *60min – x5,000*

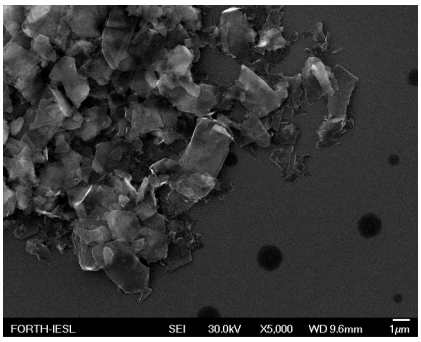

Figure 31: Chloroform – *60% applied power* – Duration *60min – x5,000*

The solvent dependence was also explored. It is observed that samples with solvent water - ethanol (3:2) and water present flakes of a smaller surface compared to the sample with solvent chloroform. The result does not correlate with any obvious solvent parameters and needs further investigation.

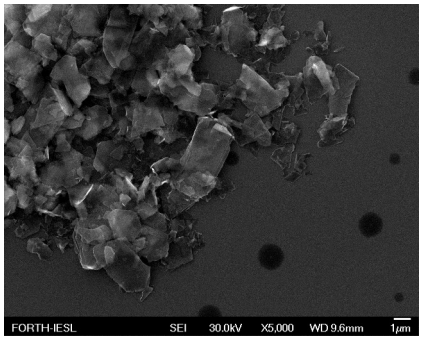

Figure 32: Chloroform – *60% applied power* – Duration *60min – x5,000*

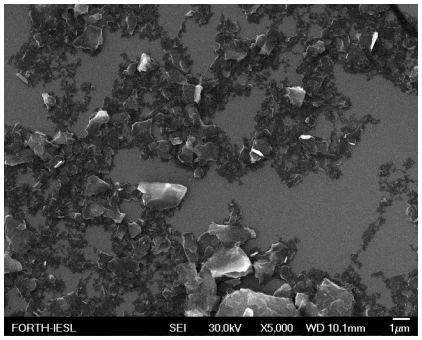

Figure 33: Water-Ethanol (3:2) – *60% applied power* – Duration *60min – x5,000*

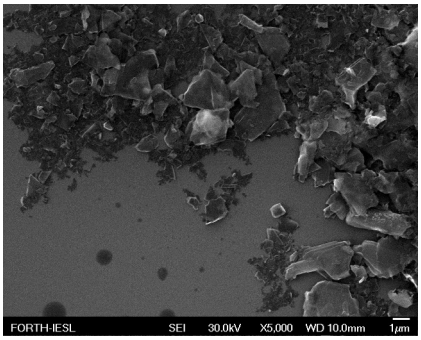

Figure 34: Water – *60% applied power* – Duration *60min – x5,000*

In this work the chosen parameters to further explore the electrical characterization of relative humidity sensors and their dependence to their flake size are 60% applied power, solvent chloroform and duration of sonication of 5 and 60 minutes.

3.3.2 Fabrication of interdigitated electrodes (IDEs)

The fabrication process of IDEs using photolithography is presented in the following table:

Table 3: Analytical procedure of photolithography

Step	***Procedure***	***Parameters***
1	Cleaning microscope slide	The chemicals were used sequentially: acetone, propanol and water
2	Oxygen plasma treatment	2 minutes, power 90 Watts and vacuum 300 mTorr
3	Deposition of the chemical HMDS	Spin coating 5000 rpm for 30 seconds
4	Stabilization of HMDS	Hot plate at 107.5 °C for 60 seconds
5	Deposition of negative resist AZ2020	Spin coating 4000 rpm for 30 seconds
6	Stabilization of resist	Hot plate at 107.5 °C for 1 minute and 30 seconds
7	Exposure to UV light	Exposure for 8 seconds, power 9 mWatt/cm^2
8	Polymerization – activation of the negative resist	Hot plate at 107.5 °C for 1 second
9	Developing the pattern	Developer MIF 826 for 25 seconds

To carry out the gold physical vapor deposition process it is important to create a vacuum of 7 x 10^{-7} Torr which is made possible by a mechanical followed by a cryogenic pump. First the sample is exposed to chromium Cr, to create a 2 nm layer as the bonding of Au to the substrate is enhanced. Gold is then evaporated and a 200 nm layer is created. The resulting pattern is shown in fig. 35.

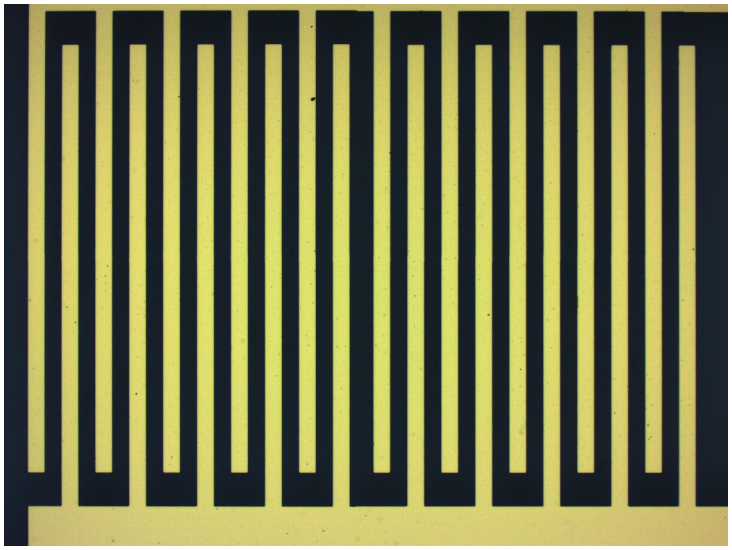

Figure 35: IDEs before deposition

3.3.3 Deposition of the material

In this work a parametric study for the deposition of the material is performed. Initially the method of the deposition is explored between dip coating and spin coating, as also the choice of rounds per minutes for the spin coating. The sample fabricated using chloroform as solvent and was sonicated at 60% applied power for 60 minutes. Oxygen plasma treated silicon substrates are used and the deposition of the suspension was done by 3 drops using pipettes Pasteur.

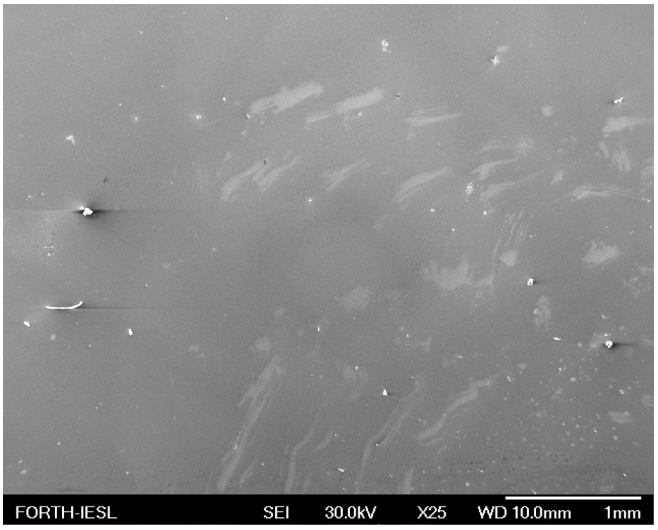

Figure 36: Dip coating

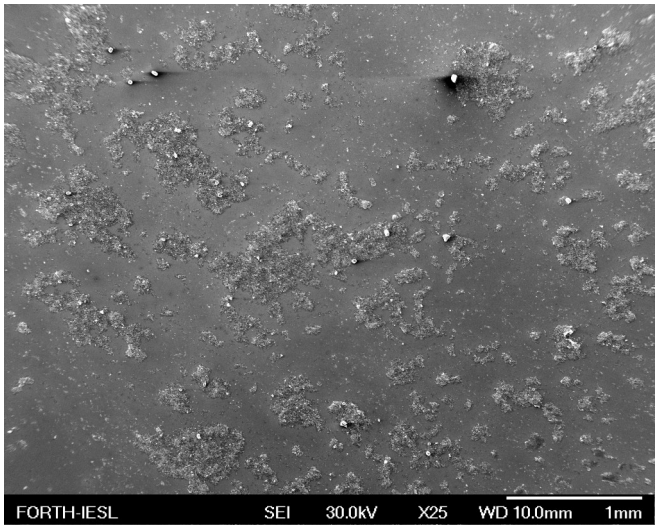

Figure 37: Spin coating – 1000 rpm

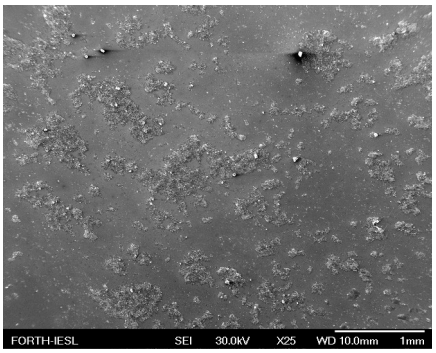

Figure 38: Spin coating – 1000 rpm

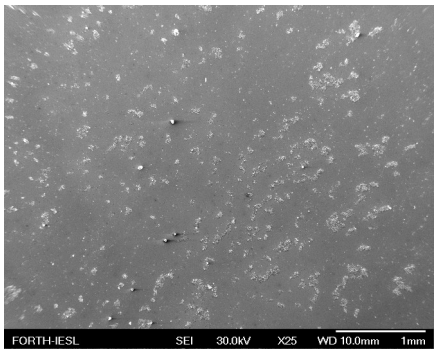

Figure 39: Spin coating – 1500 rpm

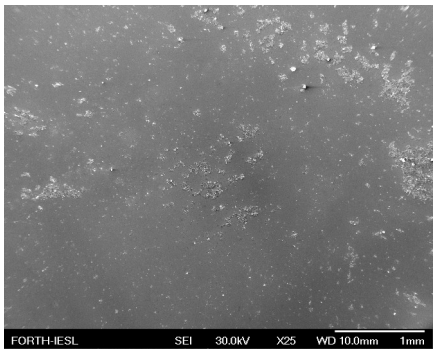

Figure 40: Spin coating – 2000 rpm

The optimum coating of the material is thicker and more dense than the resulting pictures shown above. So for the second run we choose the denser deposition technique so far – spin coating 1000 rpm, we double the concentration of the sample and we explore the quantity of the deposited material by repeating the spin coating procedure for each sample 1, 3, 5 and 8 times.

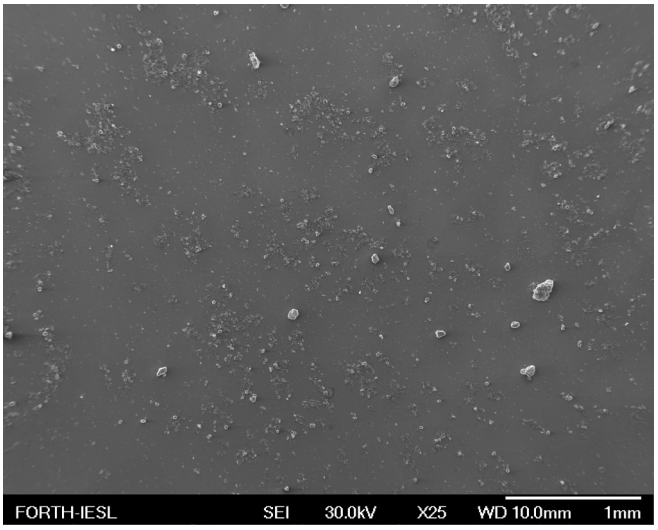

Figure 41: Spin coating – 1000 rpm – 1 repetition

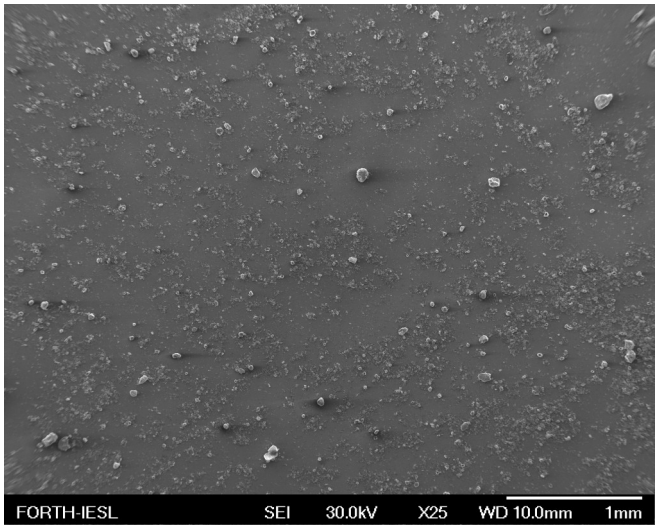

Figure 42: Spin coating – 1000 rpm – 3 repetitions

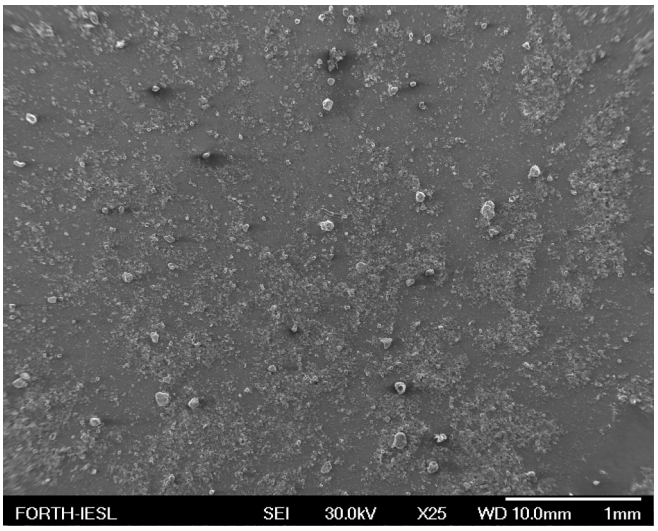

Figure 43: Spin coating – 1000 rpm – 5 repetitions

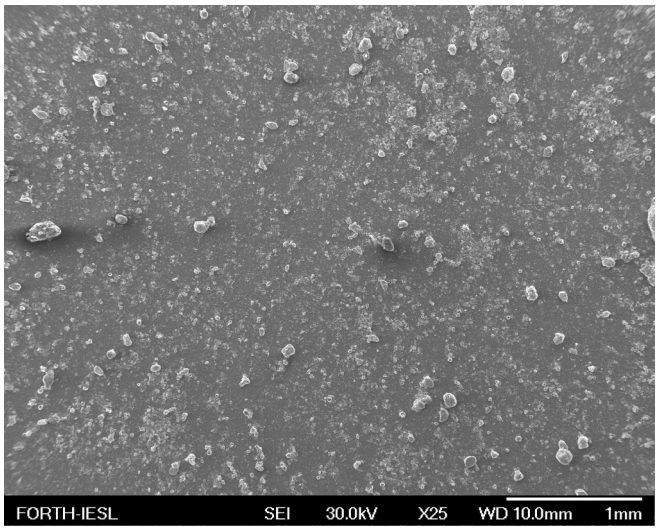

Figure 44: Spin coating – 1000 rpm – 8 repetitions

Finally the chosen parameters for the deposition of the material onto the IDEs are spin coating at 1000 rpm for 10 and 20 repetitions for a sample sonicated for 60 minutes and spin coating at 1000 rpm for 20 repetitions for a sample sonicated for 5 minutes. This selection was made so we can explore the electrical behavior dependence of the sensor changing the density and the flake size of the two dimensional material. The fabricated sensors are shown in fig. 45.

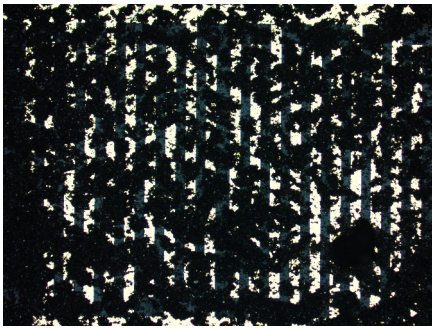

Figure 45: Optical picture of sensor 60min 10drops

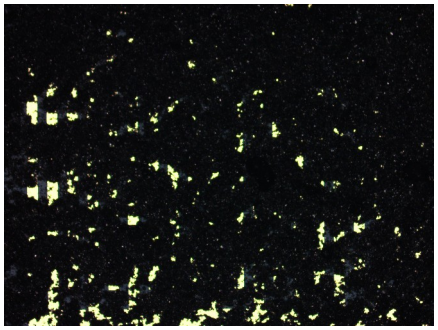

Figure 46: Optical picture of sensor 60min 20drops

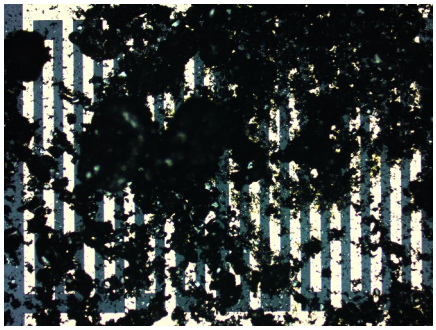

Figure 47: Optical picture of sensor 5min 20drops

3.4 Electrical characterization of the sensors

3.4.1 Humidity dependence I-V characterization

In order to explore the sensitivity for each sensor, we perform I-V measurements at the stable temperature of 25° Celsius. By sweeping the voltage from 0 to 1 Volts, we measure the current for four different relative humidity values.

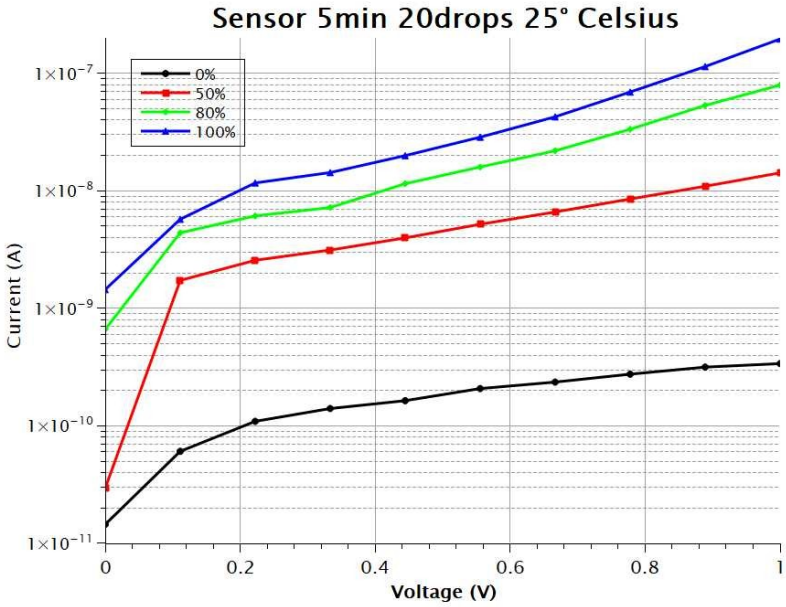

Figure 48: I-V characterization for different relative humidity values: sensor 5 minutes 20 drops 25° Celsius

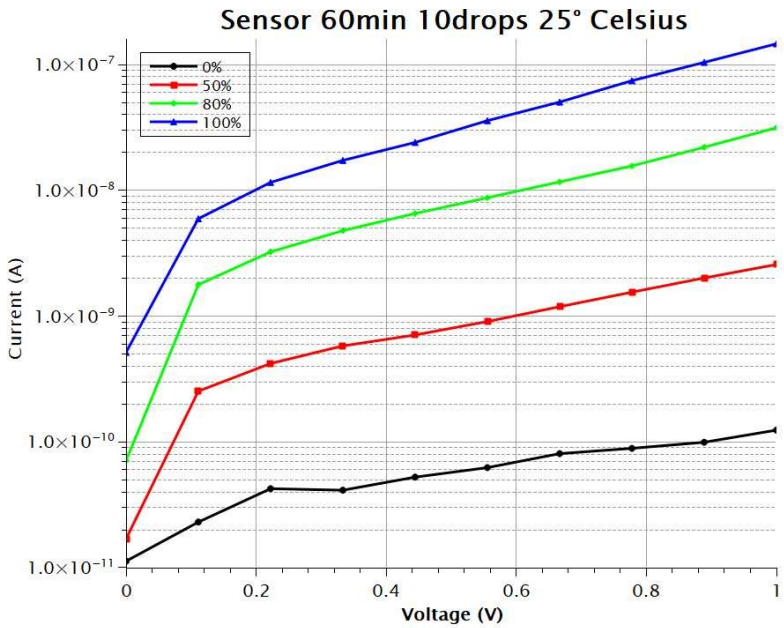

Figure 49: I-V characterization for different relative humidity values: sensor 60 minutes 10 drops 25° Celsius

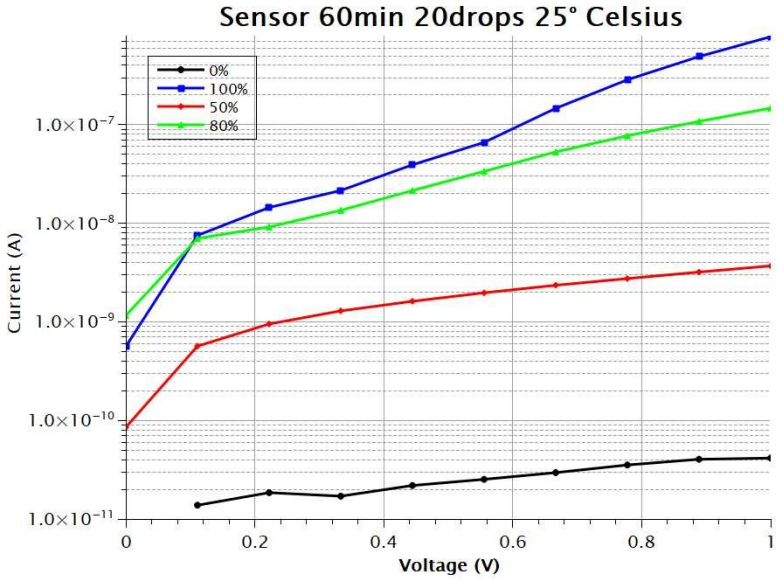

Figure 50: I-V characterization for different relative humidity values: sensor 60 minutes 20 drops 25° Celsius

As we expected, at lower humidity the conductance of the sensors are lower and as we increase the relative humidity the material is doped by water molecules and the resistance decreases. We observe

that at low relative humidity the current has a linear dependence on voltage but as we increase the humidity, the dependence becomes exponential.

3.4.2 Temperature dependence I-V characterization

Subsequently to explore the performance of the sensors' dependence on temperature we performed I-V measurements for different temperatures keeping the value of relative humidity constant at 0% RH. The results are presented below:

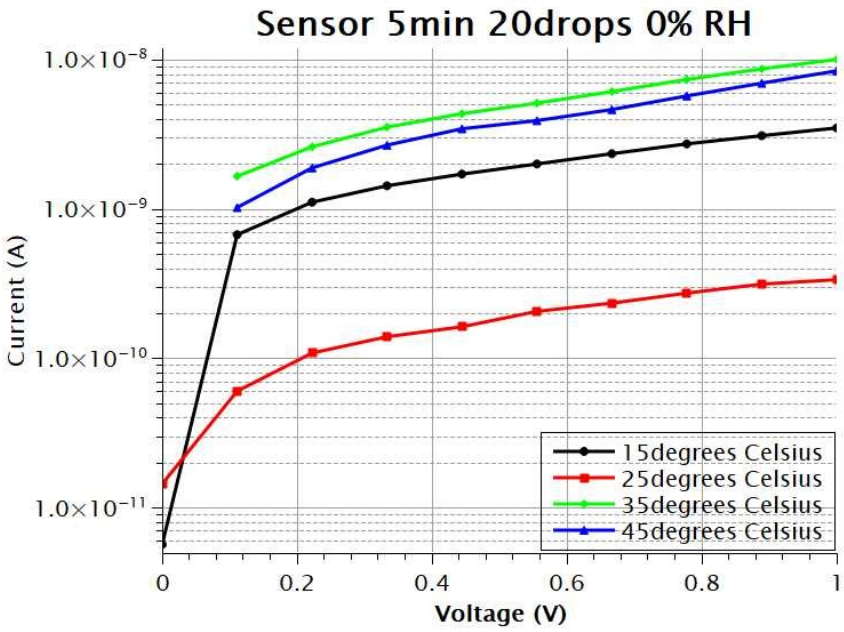

Figure 51: I-V characterization for different temperatures*: sensor 5 minutes 20 drops 0% RH*

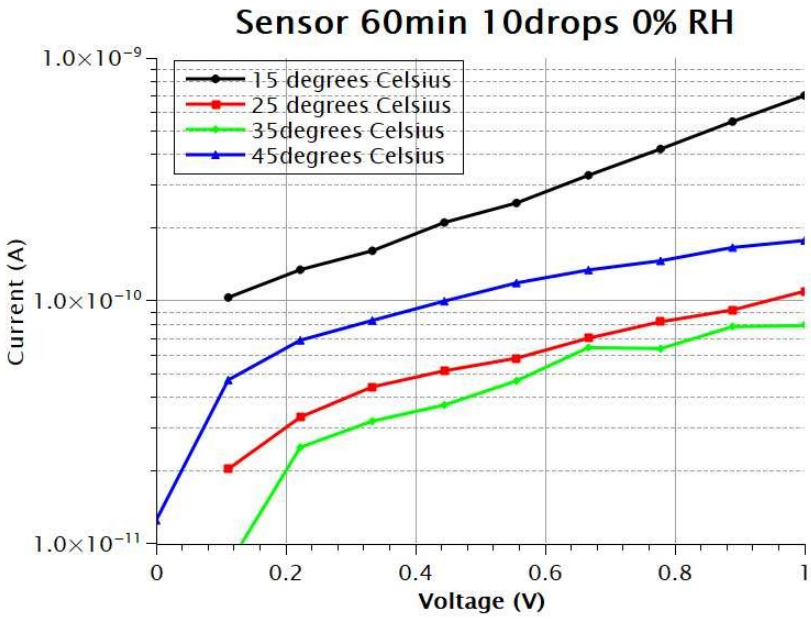

Figure 52: I-V characterization for different temperatures*: sensor* 60 *minutes 10 drops 0% RH*

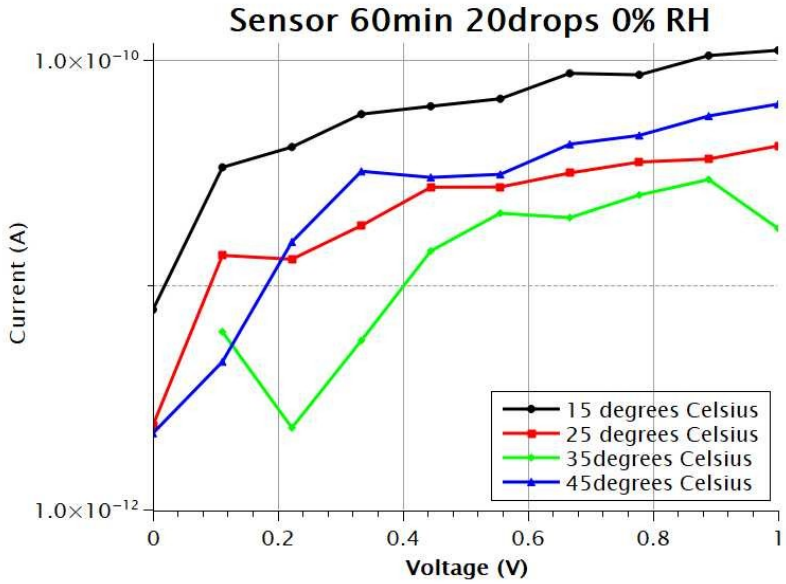

Figure 53: I-V characterization for different temperatures*: sensor 60 minutes 20 drops 0% RH*

We observe that there is not a systematic connection through our data, between the temperature and the conductance of our sensors. In order to understand the results, there is need of further investigation.

Also we explore the responsivity from 0%RH to the maximum relative humidity value through time for different temperatures.

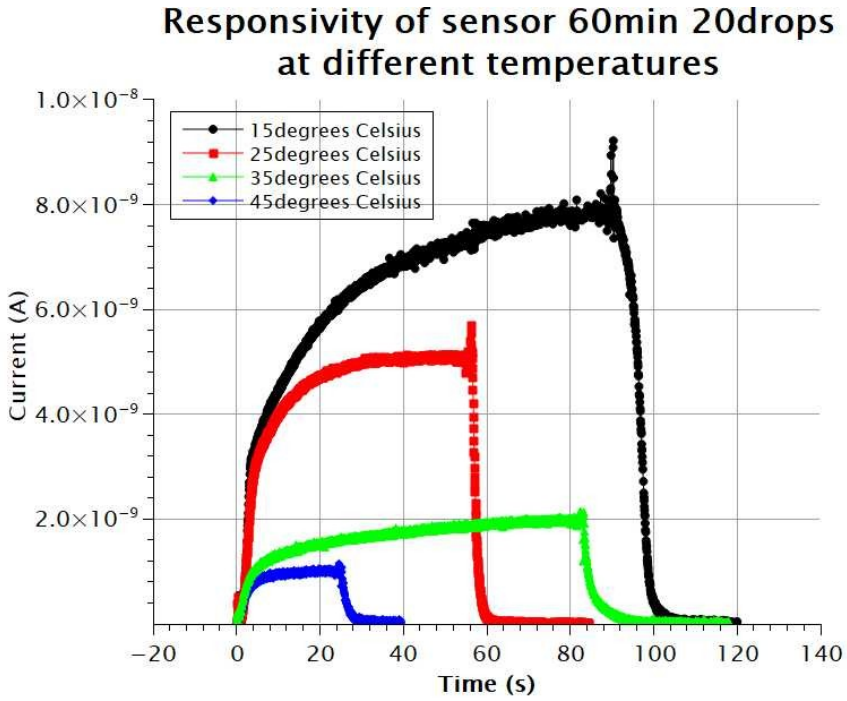

Figure 54: Temperature dependence of responsivity – sensor 60 minutes 20 drops

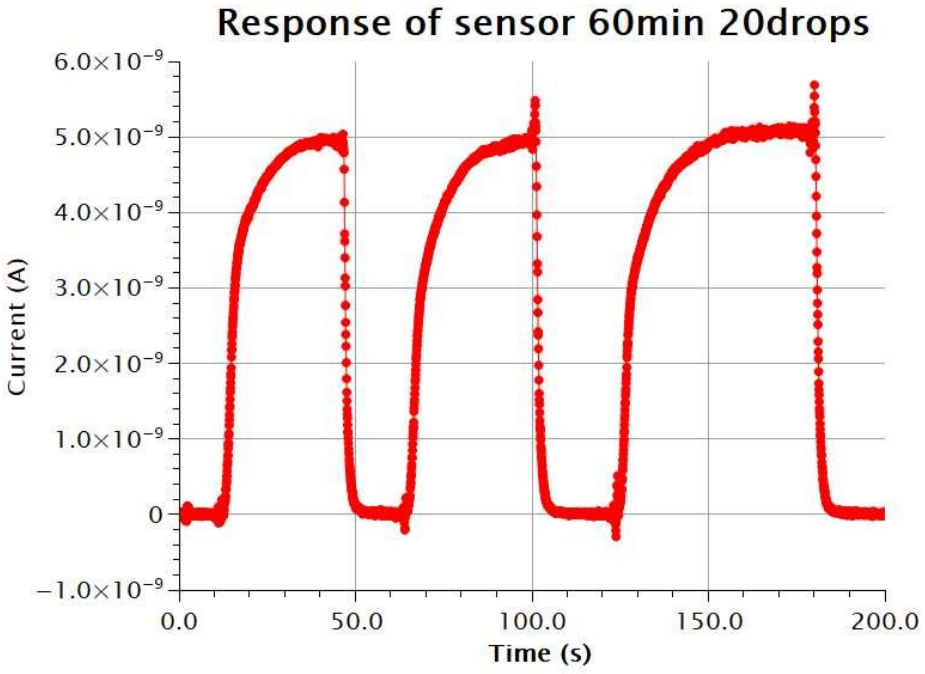

Figure 55: Response of sensor 60min 20 drops through time at 25° Celsius

We observe that the recovery time is much shorter than the response time due to the hydrophobic nature of the material. It is important to note that the maxima of the plots are very different in every temperature because currently at high temperatures the home-made humidity control set up can not reach a relative humidity of 100%.

3.4.3 Fabrication parameters dependence I-V characterization

Finally in order to connect the fabrication parameters with the electrical performance, we present I-V characterization of the three sensors at 25°C and 0% RH in fig. 56 and the sensitivity of the three sensors in fig. 57.

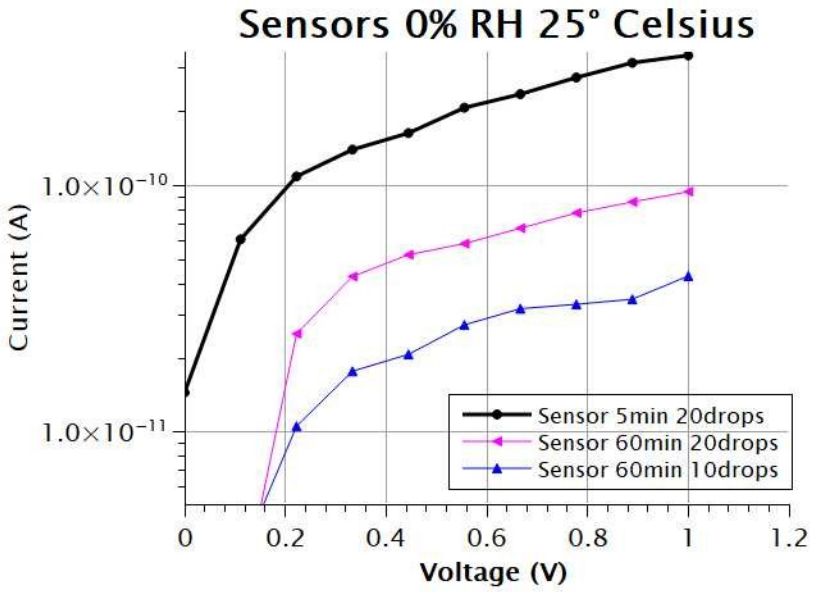

Figure 56: I-V characterization for 3 different sensors at 25°C and 0%RH

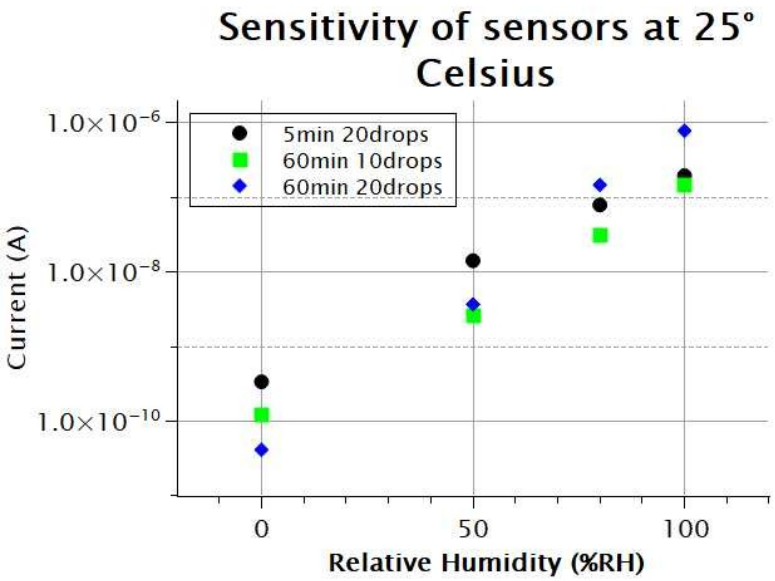

Figure 57: Sensitivity of the sensors at 25° Celsius

The sensor that has been exfoliated for 60 minutes and has 20 drops exhibits the highest sensitivity. We conclude that the more dense and smaller the flakes of the material, the higher the sensitivity of the relative humidity sensor.

Finally a comparison of response and recovery times between the sensors was made and is presented in fig. 58 and 59.

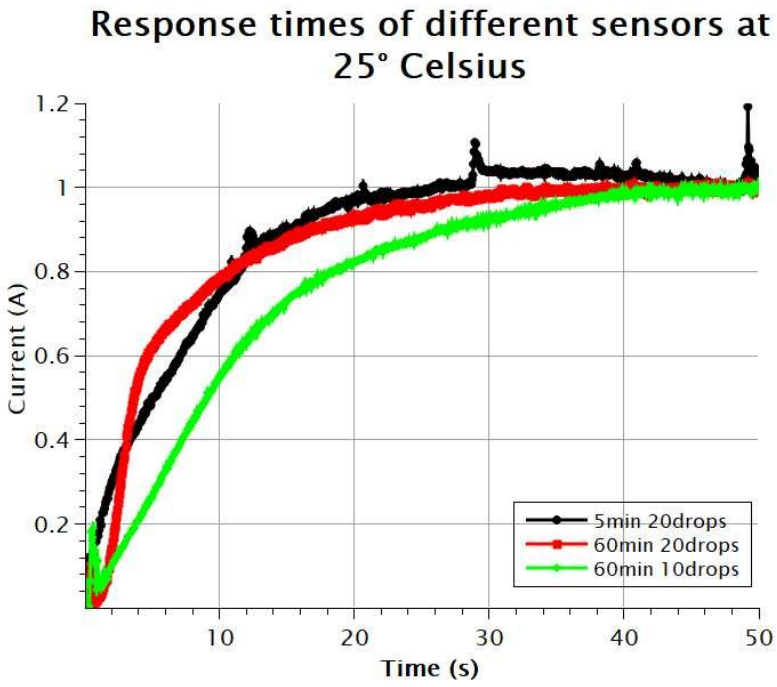

Figure 58: Response times for all sensors at 25°C

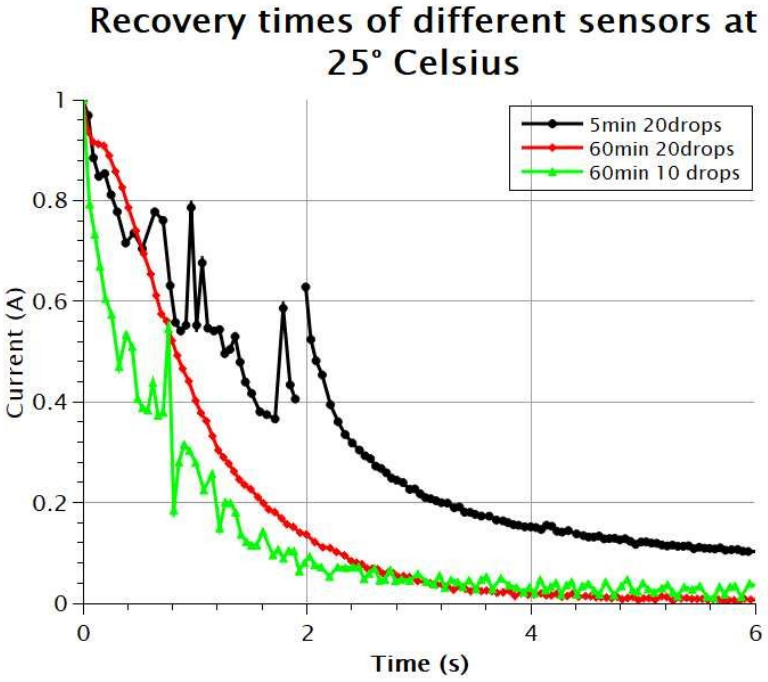

Figure 59: Recovery times for all sensors at 25°C

3.4.4 EIS characterization

Electrical impedance spectroscopy was performed in our sensors using the home-made EIS set up. In order to explore the conducting mechanisms taking place as a function of the fabrication process, and as a result of the flake size, we present the comparison of the two sensors – the one sonicated for 5 minutes and the other one for 60 minutes in figures 60 and 61. It is important to note that at the Nyquist plots below the higher frequencies are to the left of the x-axis, as the lower frequencies are to the right, as mentioned in section 2.3. The linear part of the Nyquist plot corresponds to diffusion phenomena, and the semicircular corresponds to the capacitance. As we can see, the sensor with the larger flake size presents diffusion phenomena at higher frequencies compared to the sensor with the smaller flake size.

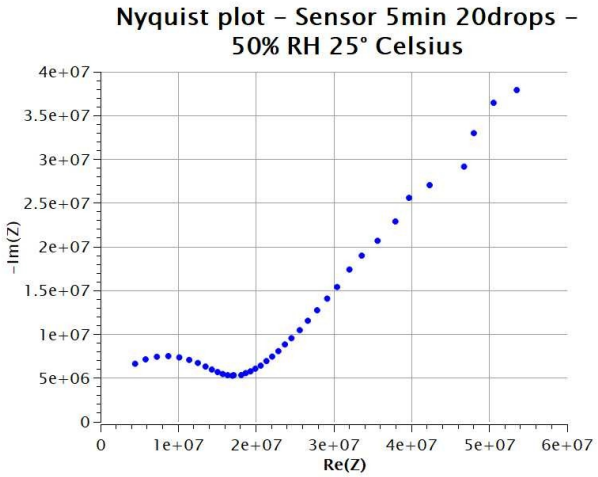

Figure 60: Nyquist plot of sensor 5 minutes 20drops 50%RH 25°Celsius

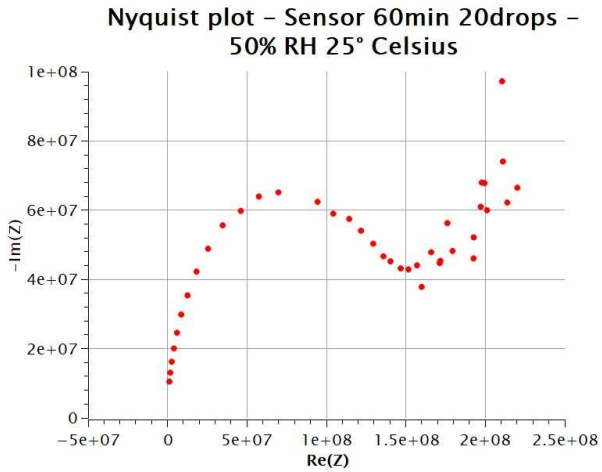

Figure 61: Nyquist plot of sensor 60 minutes 20drops 50%RH 25°Celsius

Subsequently, in order to explore the main conducting mechanism as the relative humidity increases, we perform EIS measurements at the same temperature of 25° Celsius and 100% RH. The results for both our sensors are presented in figures 62-65. We observe that as the relative humidity increases, the diffusion becomes the dominant phenomenon in the biggest part of the frequency range we measured, therefore the main conduction mechanism as we increase the relative humidity is doping.

The design of an equivalent circuit model is not trivial. We observe that the imaginary part of the impedance in the Nyquist plots do not reach zero as described in section 2.3, therefore we can not easily extract values for the resistors R_1 and R_2, using the Randles circuit model. Thus, the procedure of simulating the sensors with an equivalent circuit needs further investigation.

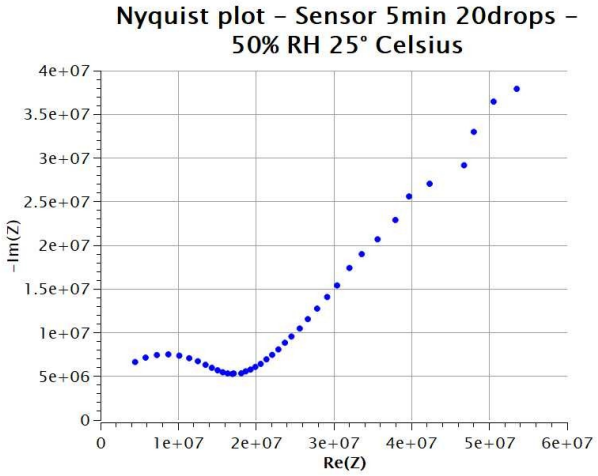

Figure 62: Nyquist plot of sensor 5 minutes 20drops 50%RH 25°Celsius

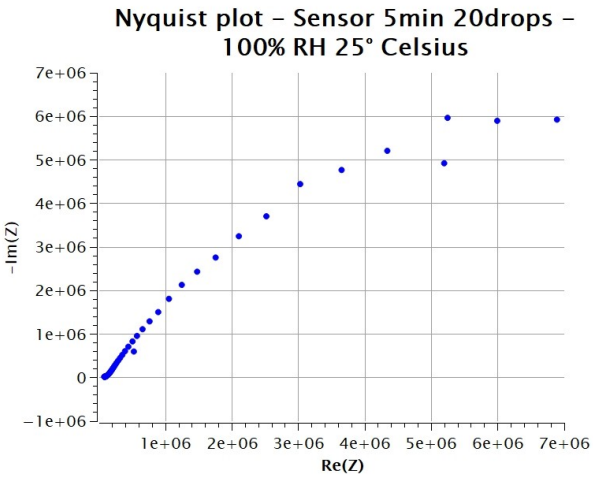

Figure 63: Nyquist plot of sensor 5 minutes 20drops 100%RH 25°Celsius

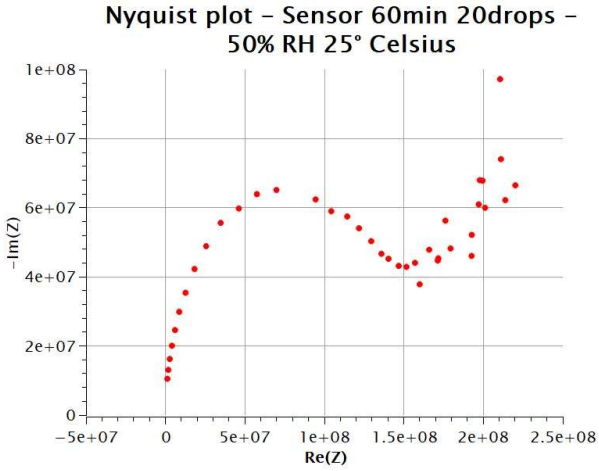

Figure 64: Nyquist plot of sensor 60 minutes 20drops 50%RH 25°Celsius

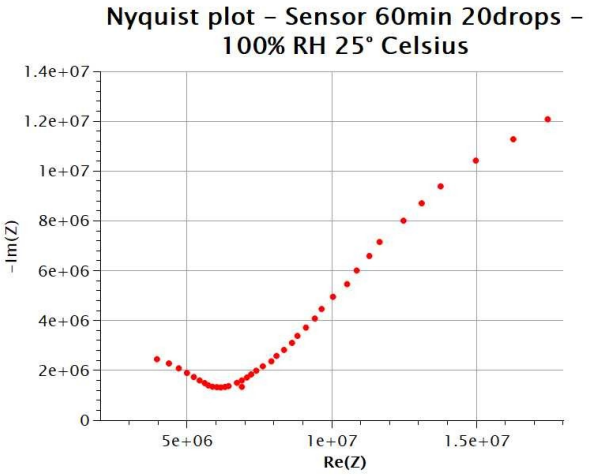

Figure 65: Nyquist plot of sensor 60 minutes 20drops 100%RH 25°Celsius

4 Discussion

In this work, we created an EIS set up, studied the deposition of $NiPS_3$, and performed a parametric study of the fabrication procedure of $NiPS_3$ relative humidity sensors and their electrical characteristics dependence. Performing I-V characterization enables us to explore key characteristics of the sensors such as sensitivity and response and recovery times, as a function of relative humidity, temperature and fabrication process, while EIS technique allows us to elucidate the dominant operating principle as a function of flake size and relative humidity.

Summarizing, we showed that the two-dimensional material $NiPS_3$ presents high sensitivity to relative humidity and very short recovery times compared to the response times, due to its hydrophobic behavior. We observed that a sensor made with a higher density and smaller flakes presents higher sensitivity and this might be due to the existence of higher amount of active sites in the perimeter of flakes, as the size of the flakes decreases. Lastly performing EIS measurements we conclude that a sensor made of larger flakes exhibits diffusion at higher frequencies, and at higher relative humidity values, diffusion dominates the conduction at most frequencies studied with EIS.

A potential direction for future work would be to perform EIS characterization at even higher frequencies, and explore the design of an equivalent circuit model regarding the results of the EIS measurements. The representation of the sensor by a circuit consisting passive elements allows a more systematic study of the conducting mechanisms, through the values of the passive elements consisting the equivalent circuit.

Bibliography

1 Olfa Kanoun, *Impedance Spectroscopy Advanced Applications: Battery Research, Bioimpedance, System Design*, 2019, https://doi.org/10.1515/9783110558920.

2 Adeline Huiling Loo et al., "Exfoliated Transition Metal Dichalcogenides (MoS2, MoSe2, WS2, WSe2): An Electrochemical Impedance Spectroscopic Investigation," *Electrochemistry Communications* 50 (January 2015): 39–42, https://doi.org/10.1016/j.elecom.2014.10.018.

3 Lorenzo A. Buscaglia, Osvaldo N. Oliveira, and Joao Paulo Carmo, "Roadmap for Electrical Impedance Spectroscopy for Sensing: A Tutorial," *IEEE Sensors Journal* 21, no. 20 (October 15, 2021): 22246–57, https://doi.org/10.1109/JSEN.2021.3085237.

4 Bobby Pejcic and Roland De Marco, "Impedance Spectroscopy: Over 35 Years of Electrochemical Sensor Optimization," *Electrochimica Acta* 51, no. 28 (September 2006): 6217–29, https://doi.org/10.1016/j.electacta.2006.04.025.

5 Daniel-Ioan Stroe et al., "Lithium-ion Battery Power Degradation Modelling by Electrochemical Impedance Spectroscopy," *IET Renewable Power Generation* 11, no. 9 (July 2017): 1136–41, https://doi.org/10.1049/iet-rpg.2016.0958.

6 Uwe Tröltzsch, Olfa Kanoun, and Hans-Rolf Tränkler, "Characterizing Aging Effects of Lithium Ion Batteries by Impedance Spectroscopy," *Electrochimica Acta* 51, no. 8–9 (January 2006): 1664–72, https://doi.org/10.1016/j.electacta.2005.02.148.

7 https://nistdigitalarchives.contentdm.oclc.org/digital/collection/p15421coll3/id/851/

8 Handeoarndd C P Hedlin, "A Study of the Accuracy of Dunmore Type Humidity Sensors," n.d.

9 Chen, Zhi, and Linge Xiao. "Humidity Sensors: A Review of Materials and Mechanisms." Sensor Letters 3 (December 1, 2005). https://doi.org/10.1166/sl.2005.045.

10 Ramesh Naidu Jenjeti, Rajat Kumar, and S. Sampath, "Two-Dimensional, Few-Layer NiPS3 for Flexible Humidity Sensor with High Selectivity," *Journal of Materials Chemistry A* 7, no. 24 (June 18, 2019): 14545–51, https://doi.org/10.1039/C9TA03214B.

11 "Pt Decorated MoS2 Nanoflakes for Ultrasensitive Resistive Humidity Sensor - IOPscience," accessed July 2, 2023, https://iopscience.iop.org/article/10.1088/1361-6528/aaa79d/meta.

12 Aashi Gupta et al., "Ultrasensitive Chemiresistive Humidity Sensor Based on Gold Functionalized WS2 Nanosheets," *Sensors and Actuators A: Physical* 331 (November 1, 2021): 113008, https://doi.org/10.1016/j.sna.2021.113008.

13 Vivek Adepu et al., "A Highly Electropositive ReS2 Based Ultra-Sensitive Flexible Humidity Sensor for Multifunctional Applications," *New Journal of Chemistry* 45, no. 13 (April 6, 2021): 5855–62, https://doi.org/10.1039/D1NJ00064K.

14 Yu Feng et al., "TaS2 Nanosheet-Based Ultrafast Response and Flexible Humidity Sensor for Multifunctional Applications," *Journal of Materials Chemistry C* 7, no. 30 (August 1, 2019): 9284–92, https://doi.org/10.1039/C9TC02785H.

15 Rajat Kumar, Ramesh Naidu Jenjeti, and Srinivasan Sampath, "Bulk and Few-Layer 2D, p-MnPS3 for Sensitive and Selective Moisture Sensing," *Advanced Materials Interfaces* 6, no. 20 (2019): 1900666, https://doi.org/10.1002/admi.201900666.

16 K. S. Novoselov et al., "Electric Field Effect in Atomically Thin Carbon Films," *Science* 306, no. 5696 (October 22, 2004): 666–69, https://doi.org/10.1126/science.1102896.

17 Max C. Lemme et al., “2D Materials for Future Heterogeneous Electronics,” *Nature Communications* 13, no. 1 (March 16, 2022): 1392, https://doi.org/10.1038/s41467-022-29001-4.

18 Ramesh Naidu Jenjeti et al., “Field Effect Transistor Based on Layered NiPS 3,” *Scientific Reports* 8, no. 1 (June 5, 2018): 8586, https://doi.org/10.1038/s41598-018-26522-1.

19 Junwei Chu et al., “High-Performance Ultraviolet Photodetector Based on a Few-Layered 2D NiPS3 Nanosheet,” *Advanced Functional Materials* 27, no. 32 (2017): 1701342, https://doi.org/10.1002/adfm.201701342.

20 Naziah M. Latiff et al., “Cytotoxicity of Layered Metal Phosphorus Chalcogenides (MPXY) Nanoflakes; FePS3, CoPS3, NiPS3,” *FlatChem* 12 (November 1, 2018): 1–9, https://doi.org/10.1016/j.flatc.2018.11.003.

22 Buscaglia, Lorenzo A., Osvaldo N. Oliveira, and Joao Paulo Carmo. “Roadmap for Electrical Impedance Spectroscopy for Sensing: A Tutorial.” IEEE Sensors Journal 21, no. 20 (October 15, 2021): 22246–57. https://doi.org/10.1109/JSEN.2021.3085237.